

Dynamic persistence of intracellular bacterial communities of uropathogenic *Escherichia coli* in a human bladder-chip model of urinary tract infections

Authors: Kunal Sharma, Neeraj Dhar^{*&}, Vivek V. Thacker^{*&}, Thomas M. Simonet, François Signorino-Gelo, Graham Knott, John D. McKinney^{*}

Affiliations:

School of Life Sciences, Swiss Federal Institute of Technology in Lausanne (EPFL), 1015 Lausanne, Switzerland.

[&] These authors contributed equally

^{*}Correspondence to: neeraj.dhar@epfl.ch, vivekvthacker@gmail.com , john.mckinney@epfl.ch

Abstract

Uropathogenic *Escherichia coli* (UPEC) proliferate within superficial bladder umbrella cells to form intracellular bacterial communities (IBCs) during early stages of urinary tract infections. However, the dynamic responses of IBCs to host stresses and antibiotic therapy are difficult to assess *in situ*. We develop a human bladder-chip model wherein umbrella cells and bladder microvascular endothelial cells are co-cultured under flow in urine and nutritive media respectively, and bladder filling and voiding mimicked mechanically by application and release of linear strain. Using time-lapse microscopy, we show that rapid recruitment of neutrophils from the vascular channel to sites of infection leads to swarm and neutrophil extracellular trap formation but does not prevent IBC formation. Subsequently, we tracked bacterial growth dynamics in individual IBCs through two cycles of antibiotic administration interspersed with recovery periods which revealed that the elimination of bacteria within IBCs by the antibiotic was delayed, and in some instances, did not occur at all. During the recovery period, rapid proliferation in a significant fraction of IBCs reseeded new foci of infection through bacterial shedding and host cell exfoliation. These insights reinforce a dynamic role for IBCs as harbours of bacterial persistence, with significant consequences for non-compliance with antibiotic regimens.

Keywords: bladder-chip, uropathogenic *Escherichia coli* (UPEC), intracellular bacterial communities (IBCs), bacterial persistence, antibiotic treatment, neutrophil swarms, neutrophil extracellular traps, shear stress, stretching, confocal live-cell imaging

Introduction

Urinary tract infections (UTIs), the second most-common cause for the prescription of antibiotics (Foxman, 2010) are characterized by the high frequency of recurrence, defined as a reappearance of infection within 12 months despite the apparently successful completion of antibiotic therapy. Recurrence occurs in about 25% of all UTIs (Foxman et al., 2000) and strongly impacts the cost of healthcare and reduces the quality of life, particularly since more than 60% of women are diagnosed with a UTI at least once in their lifetime (Klein and Hultgren, 2020). Uropathogenic *Escherichia coli* (UPEC), the causative agent for the majority of UTIs, exhibits a complex lifestyle in the bladder, with planktonic sub-populations within the urine co-existing with intracellular bacteria. UPEC invasion of the urinary bladder generates substantial changes to bladder morphology and a robust immune response. Much of our current understanding of early stages of UTI and the intracellular lifestyle is derived from studies in the mouse model (Anderson et al., 2003; Duraiswamy et al., 2018; Hannan et al., 2012; Hung et al., 2009; Justice et al., 2004; Schwartz et al., 2011; Yang et al., 2019). Examinations of mouse bladder explants via microscopy have revealed the formation of intracellular bacterial communities (IBCs) composed of thousands of bacteria within individual superficial bladder cells (Justice et al., 2004). IBCs also play a prominent role in clinical infection and have also been harvested from the urine of cystitis patients (Robino et al., 2013; Rosen et al., 2007). These structures are considered to have a linear progression from an early stage of colonization by single bacteria to an intermediate stage of biofilm-like communities culminating in the release of bacteria at the late stage (Anderson et al., 2003; Justice et al., 2004). However, long-term imaging of infected animals or of explant-tissue is technically challenging and therefore it has been difficult to capture the dynamic changes that underlie the formation of these structures and their impact on infection and clearance by subsequent antibiotic treatment.

In addition, the bladder is an extremely complex organ; it has a stratified architecture with well-differentiated cell types; a lumen filled with urine whose composition and chemical properties can vary depending on the physiological state of the individual and is subjected to periodic and large changes in organ volume and surface area (Korkmaz and Rogg, 2007). These features may play important roles in infection, but they have been hitherto hard to capture outside of a whole animal model, where they are present in their entirety and cannot be dissected in a modular manner.

Organotypic models are well-suited to address these outstanding questions. A key strength of advanced organotypic models such as organs-on-chip (Benam et al., 2016; Huh et al., 2010a; Jang et al., 2013, 2019; Kim et al., 2016; Novak et al., 2020; Zhou et al., 2016) or organoids (Cakir et al., 2019; Clevers, 2016; Rossi et al., 2018; Sato et al., 2009) is that they increasingly recapitulate the complexity of host physiology. Organ-on-chip models have been developed for several organs either in isolation or in combination (Novak et al., 2020; Ronaldson-Bouchard and Vunjak-Novakovic, 2018). These systems are increasingly being used to model infectious diseases including viral and bacterial infections of the respiratory tract (Nawroth et al., 2020; Si et al., 2021; Thacker et al., 2020, 2021), gut (Jalili-Firoozinezhad et al., 2019; Kim et al., 2016; Shah et al., 2016; Tovaglieri et al., 2019), kidney (Wang et al., 2019), and liver (Kang et al., 2017). Recently, bladder organoids that mimic the stratified architecture of the urothelium have been used to study infections (Horsley et al., 2018; Smith et al., 2006; Sharma et al., 2020). However, the organoid model suffers from certain shortcomings inherent to the 3-D architecture such as the lack of vasculature, the inability to manipulate the cells mechanically, and the constrained volume of the lumen. In contrast, organ-on-chip models offer a complementary

approach that does not suffer from these limitations. However, to our knowledge, there have been no reports of a bladder-on-chip model. Although there are studies that have developed *in vitro* bladder models that recreate the stratified architecture of the bladder epithelium (Horsley et al., 2018; Smith et al., 2006; Suzuki et al., 2019), they have not been used to recapitulate the multiple stages of IBC formation. Similarly, while a few studies have visualized different stages of IBC development by culturing human bladder cells under urine flow, these models are restricted to monoculture experiments (Andersen et al., 2012; Iosifidis and Duggin, 2020). Furthermore, the lack of vasculature in these models restricts the extent to which immune cell components or drugs can be introduced in a physiologically relevant manner and none of the systems reported to date offer the possibility of mimicking the mechanics of filling and voiding in a functioning bladder (Andersen et al., 2012; Horsley et al., 2018; Iosifidis and Duggin, 2020; Smith et al., 2006).

Here we report the development and characterization of a bladder-chip model that mimics the bladder architecture by co-culture of a well-characterized human bladder epithelial cell line with bladder microvascular endothelial cells in a device geometry that allows the two cell types to be exposed to urine and nutritive cell culture media, respectively. The flow rates in the apical and vascular channels can be controlled independently, and multiple rounds of micturition are recreated via the application of a linear strain to the PDMS membrane that serves as the substrate for co-culture. Using this model, we show that diapedesis of neutrophils to sites of infection on the epithelial side can lead to the formation of neutrophil swarms and neutrophil extracellular traps (NETs), and that IBCs offer substantial protection to bacteria from antibiotic clearance. Our observations suggest that the role of IBCs in reseeding bladder infections upon cessation of

antibiotic treatment or failure to complete a course of antibiotics might be more important than previously assumed and therefore strategies aimed towards eradication of IBCs are very crucial for treatment efficacy.

Results

Reconstitution of bladder uroepithelium and bladder vasculature

We established a bladder-chip infection model by co-culturing HMVEC-Bd primary human bladder microvascular endothelial cells with the 5637 human bladder epithelial cell line (HTB-9, epithelial cells) in a novel bladder-chip approach (Figure 1A). In a small subset of experiments, primary human bladder epithelial cells (primary epithelial cells) were used in place of 5637-cells. Immunostaining verified that the epithelial and endothelial cells formed confluent monolayers (cell densities in Table 1) with high expression of junction markers such as epithelial cell adhesion molecule (EpCAM) in the epithelial cell layer, and platelet endothelial cell adhesion molecule-1 (PECAM-1) and VE-cadherin in the endothelial cell layer (Figure 1B, C, Figure 1-figure supplement 1A-H). Expression of these and other junction markers such as E-cadherin and zonula occludens-1 (ZO-1) was consistent across monocultures (Figure 1-figure supplement 2A-G).

Similarly, a majority of the epithelial cells expressed cytokeratin 7 (CK7), a general uroepithelial marker and cytokeratin 8 (CK8), a differentiated uroepithelial marker both in monoculture (Figure 1-figure supplement 2I, J) and on-chip (Figure 1B, Figure 1-figure supplement 1B, Figure 1-figure supplement 1F). Some endothelial cells were also CK7+ (Figure 1C, Figure 1-figure supplement 2H). Co-culture of bladder epithelial and bladder endothelial cells in the

human bladder-chip therefore did not alter the cellular expression patterns of these markers as compared to monocultures. We further characterized the 5637 cells in monoculture for markers for uroepithelial differentiation. 5637 cells showed high expression of uroplakin-3a (UP3a) which has been shown to be essential for UPEC infection (Figure 1-figure supplement 2K) (Martinez et al., 2000; Mulvey et al., 1998) but only a small proportion of epithelial cells were positive for the basal cell marker cytokeratin 1 (CK1), in agreement with the umbrella cell nature of the 5637 cells (Figure 1-figure supplement 2L, M) (Duncan et al., 2004; Smith et al., 2006). Overall, these observations confirmed that the bladder-chip is populated with cells that mimic the physiology of the bladder vasculature and the superficial uroepithelial cell layer, although the relatively small size of the epithelial cells is likely an artefact inherent in the 5637 cells. Further, the chip design enables the flow of media with different compositions through the epithelial and vascular channels. We used this feature to mimic bladder physiology by perfusion of diluted pooled human urine on the epithelial side and endothelial cell medium on the vascular side.

Modelling bladder filling and bladder voiding in the bladder-chip

The human bladder experiences vast changes in volume and surface area on a periodic basis. The first phase of this cycle, (*'filling bladder state'*), occurs through a slow and gradual increase in bladder volume due to addition of urine from kidney via the ureters, resulting in a large increase in bladder volume (Figure 1D). At the level of the uroepithelium, these changes manifest as a 2-dimensional biaxial stretch of the bladder tissue. *Ex vivo* studies in rat bladders report that a maximum strain of 90% and 130% can be applied to bladder explants in the circumferential and longitudinal directions (Gloeckner et al., 2002; Parekh et al., 2010), although micturition *in vivo* is likely triggered before this maximum value is reached. Subsequently, volume growth slows,

and the bladder attains a relatively constant volume, with the bladder epithelium in a corresponding state of maximal stretch, (*'filled bladder state'*). Voiding of the bladder through urination rapidly reduces bladder volume, (*'voiding bladder state'*) and removes the strain experienced by the bladder cells. The bladder epithelium, as a viscoelastic material, responds to the removal of strain and relaxes over the subsequent period (Pascalis et al., 2018) where the bladder volume remains low (*'voided bladder state'*) (Figure 1D).

The architecture of the bladder-chip device allows for a linear strain to be applied to the porous membrane via negative pressure in the channels adjacent to the main channel of the device (*'the vacuum channels'*) (Grassart et al., 2019; Huh et al., 2010b) (Figure 1A). We characterized the linear strain experienced by epithelial cells due to application of negative pressure (Figure 1-figure supplement 3). A plot of applied pressure vs. strain was linear, and we achieved a dynamic range of linear strain (0 to 19 %) by application of negative pressure (0 to -900 mbar). High levels of applied strain were incompatible with long-term time-lapse microscopy as it generated a significant drift in the axial position of the membrane. We therefore limited the linear strain applied to a maximum of 10%, which is of the same order of magnitude, albeit a small fraction of the typical strain experienced by the bladder tissue *in vivo*. We then modelled the bladder filling and voiding over a 6-hour duty cycle with different states: *filling bladder* (0 to 2 hours, 0 to 10% strain), *filled bladder* (2 to 4 hours, 10% strain), *voiding bladder* over a period of 2 minutes (4 hours to 4:02 hours, 10% to 0% strain) and *voided bladder* (4:02 hours to 6 hours, 0% strain) (Figure 1D). This 6-hour duty cycle was repeated for the remaining duration of each experiment. Overall, the bladder-chip model enables co-culture of two cell-types in nutritionally different microenvironments with an applied strain that partly mimics the physiology of bladder filling and voiding cycles.

UPEC infection of the epithelial layer under flow in the bladder-chip model

UPEC attachment and invasion of bladder epithelial cells has been shown to be sensitive to fluidic shear stress (Andersen et al., 2012; Zalewska-Piątek et al., 2020). Although UPEC infection in the bladder can occur in the presence or absence of shear stress, we infected the epithelial layer on the bladder-chip under a flow rate of 1.2 ml/hour (corresponding to a shear stress of $0.02 \text{ dyne cm}^{-2}$) for a period of 1.5 -2 hours. Low shear stress conditions have been recently reported to enhance bacterial adhesion to epithelial cells (Zalewska-Piątek et al., 2020) and likely reflects the *in vivo* environment except during urination when the shear stress increases dramatically to 3-5 dyne cm^{-2} (Sokurenko et al., 2008). This choice was also motivated by the small volumes of the microfluidic chip, as rapid bacterial growth in the diluted human urine could lead to acidification of the medium. Under these conditions, an overwhelming majority of bacteria did not attach to the epithelial cells. Time-lapse microscopy showed that bacterial attachment to the epithelial cells increased steadily over this period, but that the typical infectious dose at the end of this period was low (<1 bacterium per epithelial cell, [Figure 2-figure supplement 1](#)).

Accordingly, we established a 28-hour live-cell imaging experimental protocol as shown in the schematic in [Figure 1E](#) and described in greater detail in the subsequent sections and in the Materials and Methods. Briefly, this consisted of an initial period of acclimatization, followed by UPEC infection, introduction of neutrophils, and two consecutive cycles of antibiotic treatment and recovery to monitor IBC dynamics at the single-cell level. This experimental protocol therefore mimicked key aspects of the host-pathogen interactions in early stages of UTIs as well as the response to antibiotic treatment.

Diapedesis of neutrophils across the epithelial-endothelial barrier in response to UPEC infection in the bladder-chip

The bladder-chip platform enables continuous imaging while maintaining flow in both epithelial and vascular channels and mechanically stretching the membrane as part of the bladder voiding cycle. At the start of each live-cell imaging experiment, bladder epithelial cells in an initial relaxed state were perfused with sterile pooled human urine diluted in PBS on the epithelial side and endothelial cell medium on the vascular side respectively (Figure 2A1, B1, Figure 2-figure supplement 2A1). The epithelial side was inoculated with a low dose of UPEC in diluted urine and infection was performed under flow (Figure 2A2, B2, Figure 2-figure supplement 2A2) for ca. 1.5 to 2 hours. The first bladder duty cycle was also initiated at this timepoint. We maintained the optical focus of the microscope on the epithelial layer over the subsequent course of infection. UPEC attachment was evident during this infection phase by visual inspection (Figure 2B2, Figure 2-figure supplement 2A2).

After this period of infection, unattached bacteria in the epithelial channel were removed by perfusion of diluted urine. As our aim was to study the interaction of UPEC with host cells, this perfusion was maintained throughout the experiment. Continuous perfusion reduced the accumulation of bacteria in the urine and enabled imaging of intracellular bacteria without large amounts of background noise in the fluorescence channels from planktonic bacteria. We subsequently performed a series of interventions that mimic the course of UTI infections and used time-lapse imaging to monitor the simultaneous changes in host-pathogen interaction dynamics. Immune cells were introduced into the vascular channel to mimic the host response to

infection. Among innate immune cells, neutrophils are the first line of defense in UTIs (Haraoka et al., 1999). Neutrophils were isolated from human blood with a high degree of purity (Son et al., 2017) verified by immunostaining for the neutrophil-specific marker CD15 (Zahler et al., 1997) (Figure 2-figure supplement 3).

Neutrophils were pre-labelled with the cytoplasmic CellTrackerTM Deep Red dye to enable identification and tracking during time-lapse imaging and subsequently introduced in the bladder-chip devices through the vascular channel at a cell concentration of ca. 2 million cells/ml similar to the neutrophil concentration in human blood (Hsieh et al., 2007). This mimics the natural route of immune cell migration into the bladder (schematic in Figure 2A3-A5, snapshots in Figure 2B3-B5, Figure 2-figure supplement 2A3-A5) During this period, the flow rate through the vascular channel was increased to 3ml/hour (shear stress $\eta = 1 \text{ dyne/cm}^2$), which aids neutrophil attachment to endothelial cells (Alon et al., 1995). In uninfected control chips, neutrophil attachment to the endothelial layer was minimal (Figure 2-figure supplement 4A, B) and diapedesis of neutrophils to the epithelial layer was rare (Figure 2C, Figure 2-figure supplement 5A). In stark contrast, infection of the epithelial layer with UPEC elicited a robust attachment of neutrophils to endothelial cells (Figure 2-figure supplement 4C, D), along with rapid diapedesis across to the epithelial side (Figure 2B2-B4, Figure 2-figure supplement 2A2-A4, Figure 2-figure supplement 5C). We confirmed that neutrophil diapedesis was also stimulated in the uninfected chips upon exposure to a gradient across the epithelial-endothelial barrier of pro-inflammatory cytokines known to be upregulated during UTIs - IL1 α , IL1 β , IL-6 and IL-8, each at 100 ng/ml (Agace et al., 1993; Hedges et al., 1992; Nagamatsu et al., 2015; Song et al., 2007) (Figure 2-figure supplement 5B). However, infection elicited a more robust neutrophil diapedesis response compared to the cytokine gradient, evident in the higher number

of neutrophils observed across multiple fields of view on the epithelial side (Figure 2-figure supplement 5B-D). These results suggest that infection on-chip generates a strongly pro-inflammatory environment locally and that neutrophil diapedesis is further stimulated by the presence of UPEC (Agace et al., 1995; Oliveira et al., 2016).

Using time-lapse imaging, we quantified the kinetics of neutrophil migration with a temporal resolution of up to 7.5 minutes. Neutrophil diapedesis to the epithelial sites of infection was detected as early as ca. 15-17 minutes post-introduction into the vascular channel (Figure 2B3, Figure 2-figure supplement 2A3, Figure 2-video 1, Figure 2-video 2). Neutrophils that migrated to the epithelial side aggregated on the epithelial cells (Figure 2B4-B5, Figure 2-figure supplement 2A4-A5, Figure 2-video 1, Figure 2-video 2). In some cases, these neutrophils were able to control bacterial growth (Figure 2B4-2B5, solid yellow boxes) whereas in others, bacterial growth was uncontrolled (Figure 2B4-2B5, dashed white boxes). Diapedesis was observed in every field of view examined across infected chips (n=4), whereas diapedesis occurred infrequently in uninfected controls (Figure 2C). Furthermore, the size of these aggregates was significantly larger in infected bladder-chips vs. uninfected controls, with the large aggregates in infected-chips exhibiting the characteristic features of neutrophil swarms (Kienle and Lämmermann, 2016; Kreisel et al., 2010; Lämmermann et al., 2013). We quantified the size of the swarm-like aggregates by either estimating the maximum number of neutrophils observed in fields of view on the epithelial side (Figure 2D) or by measuring the total volume occupied by neutrophils normalized to the volume of a 3D field of view (Figure 2E). Using either metric, infection generated swarms that did not occur in uninfected bladder-chips. Time-lapse imaging confirmed that swarm formation was rapid (Figure 2F), and swarms reached their

maximum size typically between 60- and 90-minutes post-introduction of neutrophils (Figure 2G).

Formation of neutrophil extracellular traps (NETs) in response to UPEC infection

In addition to direct killing of engulfed bacteria, neutrophils, can also form neutrophil extracellular traps (NETs) through the release of cytosolic azurophilic granules around a scaffold of decondensed chromatin (Oliveira et al., 2016). These structures can trap and kill extracellular bacteria (Brinkmann et al., 2004). NETs consist of antimicrobial granules such as myeloperoxidase (Metzler et al., 2011) and neutrophil elastase (Papayannopoulos et al., 2010) and have been observed in urine harvested from UTI patients (Yu et al., 2017). Interestingly, infected bladder-chips immunostained at 2 hours post-introduction of neutrophils (3.5 hours post infection) with antibodies against neutrophil myeloperoxidase (Figure 2H, Figure 2-figure supplement 6A1-A3) and neutrophil elastase (Figure 2I, Figure 2-figure supplement 6B1-B3) showed areas on the epithelial layer which stained positive for each marker (Figure 2H3, 2I3). In each example, zooms clearly show long filament-like structures that extend between cells and are either myeloperoxidase positive (Figure 2H5) or neutrophil elastase positive (Figure 2I5), morphological features that are strongly suggestive of NETs (Brinkmann et al., 2004; Metzler et al., 2011; Papayannopoulos et al., 2010). These areas had high numbers of neutrophils – a characteristic of swarms, and many of these neutrophils did not retain strong expression of the cytoplasmic CellTracker dye (cf. Figure 2H2 and 2H3, 2I2 and 2I3), suggestive of metabolic activation. Formation of NET-like structures was also observed in some instances by neutrophils in some locations on the endothelial channel, although large swarms did not form here (Figure 2-figure supplement 6B1-B3).

288 To further characterize these structures, we imaged the epithelial layer of uninfected and infected
289 bladder-chips with or without the addition of neutrophils using scanning electron microscopy
290 (SEM). Representative images of the epithelial layers of uninfected bladder-chip controls (Figure
291 2-figure supplement 7A) contrast with those from infected bladder-chips after neutrophil
292 diapedesis (Figure 2J1-J4, Figure 2-figure supplement 7C); neutrophils on the surface of the
293 epithelial layer are clearly distinguishable by their distinctive spherical morphology and size
294 (Figure 2J1, amber arrowheads). Thick bundles consisting of many thinner fibers formed
295 between these neutrophils are shown by white arrowheads and appear to extend between
296 adjacent neutrophils (Figure 2-figure supplement 7C). Importantly, these structures did not form
297 in infected bladder-chips without the introduction of neutrophils (Figure 2-figure supplement
298 7B), confirming that the NET-like architectures identified via immunofluorescence correspond to
299 structures identified by SEM that morphologically resemble NETs (Figure 2H, I). Hereafter for
300 simplicity, we shall refer to these structures as NETs. A series of higher-magnification images in
301 Figure 2J2-J4 show the structure of the NETs in greater detail. Many individual UPEC bacteria
302 (green arrowheads) are captured in these structures (Figure 2J2-J4), which are themselves
303 composed of many individual thinner fibers (yellow arrowheads Figure 2J2-J4). In these images,
304 a majority of the epithelial cells have a characteristic flattened morphology with cell appendages
305 that can extend between cells (cyan arrowheads); this contrasts with the highly infected epithelial
306 cell that is spherical in shape and with bacteria attached to its surface (Figure 2J1, purple
307 arrowhead). Notably, we did not observe uroplakin plaques reported *in vivo* (Kong et al., 2004)
308 on the surface of uninfected or heavily infected epithelial cells in the bladder-chip model.
309 Lastly, to verify that NET formation was a direct response to UPEC and not caused by
310 hyperactivation of neutrophils due to experimental handling, we collected the neutrophils that

passed through an infected bladder-chip without attachment. Even upon infection, an overwhelming majority of the cells perfused into the chip flow out without adhering, because of the geometry of the channels in the device. NET formation in these neutrophils was not observed unless the neutrophils were themselves infected by UPEC shed from the bladder-chip (Figure 2-figure supplement 8). The bladder-chip model is therefore able to recapitulate key aspects of the host response to the early stages of UPEC infection while demonstrating that intracellular bacteria were substantially protected from neutrophil-mediated killing.

Heterogenous dynamics of intracellular bacterial communities within uroepithelial cells

Urinary tract infections that do not resolve upon intervention by the host immune system often require treatment with antibiotics. Antibiotics have complex pharmacokinetic and pharmacodynamic profiles *in vivo*, which we attempted to model through two successive rounds of a high dose administration of ampicillin - an antibiotic formerly prescribed for uncomplicated UTIs (ca. 40x MIC, Figure 3-figure supplement 1A), on both the epithelial and vascular side, interrupted by periods with no antibiotic (schematics in Figure 3A, 1E). Continuous time-lapse imaging over this entire period allowed us to capture the responses of bacteria to this simplified model of antibiotic profiles and to study the persistence of UPEC upon antibiotic treatment in the different physiological niches (Figure 3 and Figure 4).

A consequence of the first cycle of antibiotic administration under flow was the elimination of planktonic bacterial growth in the media in the apical channel, as is observed within the lumen of the bladder *in vivo*. Many bacteria that were still intact at the end of the antibiotic treatment intact did not regrow after the antibiotic was removed (Figure 3-figure supplement 1B). Regrowth commenced in only a small fraction of bacteria (Figure 3-figure supplement 1C) after

a variable lag phase (Figure 3-figure supplement 1D) and rapid regrowth was highly correlated with intracellular location of bacteria within epithelial cells. These bacteria subsequently grew with a variable lag period to form large intracellular structures. These structures strongly resembled intracellular bacterial communities (IBCs) reported *in vivo*. An example of an early stage of the formation of IBC-like structures is shown in the timeseries in Figure 3B1-B5, Figure 3-video 1. This IBC was initially seeded with few bacteria that are present in Figure 3B1 and clearly visible in Figure 3B2. At the end of the timeseries, the entire host cell was packed with bacteria (Figure 3B5). The exponential increase in bacterial numbers frequently led to the saturation of the 8-bit images in the bacterial channel. We also observed similar structures in infected chips reconstituted either with 5637 epithelial cells (Figure 3-figure supplement 1E, F) or primary epithelial cells (Figure 3 – figure supplement 1G-I) and treated with ca. 8X MIC of Fosfomycin (Fedrigo et al., 2017), a current frontline drug prescribed for UTIs with a different mode of action to ampicillin. This verified that the formation of these structures was independent of the host cell type and antibiotic used. Hereafter, we shall refer to these IBC-like structures as IBCs for simplicity, acknowledging that these structures may differ from IBCs reported in infected animals.

We therefore examined these structures in separate bladder-chips via immunofluorescence imaging with a higher spatial resolution (Figure 3C, Figure 3-figure supplement 2). Zooms of two of the four IBCs highlighted in Figure 3C show numerous tightly packed bacteria within epithelial cells that are both CK7+ (Figure 3C) and CK8+ (Figure 3-figure supplement 2). These bacterial morphologies are highly similar to early-stage IBCs observed in the bladder (Anderson et al., 2003; Duraiswamy et al., 2018; Justice et al., 2004). Higher resolution images of the

biofilm-like structures within IBCs obtained via correlative light (Figure 3D) and transmission electron microscopy (Figure 3E) showed that bacteria in IBCs can be either coccoid or rod shaped, which is also evident in scanning electron micrographs of bacteria within IBCs (Figure 3F). IBCs within bladder-chip model therefore show many of the distinctive morphological features reported from images of infected bladders in the mouse model (Anderson et al., 2003; Hunstad and Justice, 2010).

Numerous reports from the mouse model of infection have shown IBCs to be dynamic structures; growth in IBCs eventually culminates in bacterial shedding or the complete exfoliation of the IBC. The underlying dynamics of these phenotypes is hard to capture in the mouse model, but the bladder-chip model allowed us to track the dynamics of bacterial growth within individual IBCs over extended periods of time, providing information on bacterial dynamics within so-called early, middle, and late-stage IBCs. In experiments performed with ampicillin, the heterogeneity in growth rates is evident from the timeseries for three IBCs (Figure 3G1-G5, Figure 3-video 2). IBCs#1 and 2 subsequently began to shed individual bacteria (Figure 3G4), a phenotype not observed in IBC#3. At a later timepoint (Figure 3G5) the fates of all three IBCs were dramatically different – the cell containing IBC#1 had completely exfoliated and was removed from the field of the view by flow in the epithelial channel, IBC#2 continued to shed bacteria, whereas growth remained slow in IBC#3. We monitored the eventual fate of n=100 IBCs during the first and the second growth cycles which confirmed that shedding and exfoliation were not mutually exclusive. While some IBCs only shed bacteria (n=28) and others exfoliated without shedding (n=27), a substantial fraction of IBCs showed shedding prior to exfoliation (n=31) and some IBCs displayed neither phenotype (n=14). Furthermore, in addition

to the coccoid and rod-shaped morphologies highlighted in [Figure 3C-F](#), time-lapse imaging also enabled us to capture morphotypes that occurred relatively rarely such as the intracellular growth of filamentous forms of UPEC ([Figure 3H1-H5](#), [Figure 3-figure supplement 3](#), [Figure 3-video 3](#), [Figure 3-video 4](#)). In this time series, a filamentous bacterium can be seen and appears to encircle the inner boundary of the cell ([Figure 3H1-H4](#)) before filling the volume entirely ([Figure 3H5](#)). Overall, time-lapse imaging confirms that a significant fraction of bacteria within IBCs can survive the first round of antibiotic treatment and are the source for reseeding of both the extracellular bacterial populations as well as the subsequent growth of IBCs in newly infected cells.

Dynamic persistence of intracellular bacterial communities within uroepithelial cells

A subsequent round of antibiotic treatment provided an opportunity to study the dynamic persistence of bacteria within IBCs in response to an antibiotic profile that was a closer mimic of the periodic antibiotic exposures *in vivo*. Furthermore, at this stage of the experiment, we were also able to study the responses of bacteria in intermediate and mature late-stage IBCs to antibiotic treatment, which was not possible during the first round of antibiotic administration early in the course of infection. Owing to the complexity of long-term live-cell imaging, we focused on ampicillin treatment in chips reconstituted with the 5637 cells. We corroborated these findings with live-cell imaging and snapshots taken from chips reconstituted with 5637 cells and primary epithelial cells respectively and treated with Fosfomycin. Live-cell imaging in chips treated with ampicillin ([Figure 4A1-A5](#) and [Figure 4-video 1](#)) shows that bacterial growth after the first round of antibiotic treatment resulted in the formation of many large IBCs with tightly packed bacteria ([Figure 4A1-A2](#)). Many of the bacteria within each of the four IBCs were

eliminated by the antibiotic, but a substantial proportion of bacteria in each IBC nevertheless survived the antibiotic treatment (Figure 4A3). Each of these IBCs subsequently regrows when the antibiotic is removed (Figure 4A4-A5), and two additional IBCs are seeded during this time (Figure 4A4-A5, white arrowheads). Similar results were obtained with chips reconstituted with primary epithelial cells and treated with Fosfomycin (lower resolution whole-chip scans in Figure 4 – figure supplement 1A,B). Overall, the second round of antibiotic administration led to a sharp decline in instances of subsequent bacterial regrowth (Figure 3-figure supplement 1C). In all instances, regrowth either occurred directly within IBCs, or was caused by the shedding of bacteria from IBCs to repopulate the extracellular niche and seed new IBCs, highlighting the dynamic stability of this niche and its importance in establishing persistent infection. We therefore performed a careful analysis to quantify bacterial growth rate within IBCs. Growth within IBCs across different time periods was exponential in both epithelial cells (Figure 4B) and primary epithelial cells (Fig. 4 – figure supplement 1C). We were able to track a subset of IBCs across two growth cycles (examples in Figure 4C). In a majority of instances these revealed exponential growth in the absence of antibiotic, delayed response to antibiotic, and a lag phase after the antibiotic was removed. In general, bacterial growth in IBCs in the second growth cycle was slower than in the first (Figure 4D). However, this population level statistic may be influenced by the fact that many of the IBCs monitored in the second growth cycle had been exposed to two rounds of antibiotic treatment. For this sub-population, in n=16 out of n=18 IBCs, growth was slower after the second round of antibiotic administration (Figure 4E). Next, we examined the dynamics of bacterial growth within IBCs during the period of antibiotic treatment in greater detail. In the IBC shown in the timeseries in (Figure 4F1-F5, Figure 4-figure supplement 2A1-A5, Figure 4-video 2, Figure 4-video 3), growth before antibiotic administration

(Figure 4F1-F2) continued for a considerable period after the antibiotic was administered (Figure 4F3-F4, Figure 4-figure supplement 2A1-A3). Eventually, a reduction in bacterial volume towards the end of the antibiotic administration period was observed (Figure 4F5, Figure 4-figure supplement 2A4-A5). In contrast, the relatively smaller IBC in the timeseries in Figure 4G1-G5, Figure 4-figure supplement 2B2-B5, Figure 4-video 4, Figure 4-video 5 continued to grow throughout the period of antibiotic administration. These different dynamics are also captured in the plot of bacterial volume for multiple IBCs before, during, and after the antibiotic treatment (Figure 4H). In all cases, bacterial volume continues to increase during a significant period of antibiotic administration and in 2 out of 18 cases, there was no decrease in bacterial volume throughout this period (Figure 4H). In contrast, extracellular bacteria likely adherent on the epithelial cells but not internalized within them were rapidly eliminated by combination of antibiotic treatment and flow (Figure 4J), in all cases the bacterial volume reduced immediately upon antibiotic administration. Fosfomycin treatment elicited a rapid decline in both extracellular bacterial volume and bacterial volume in IBCs, consistent with the greater cellular penetrance of this antibiotic (Figure 4I). This differential clearance of bacteria was therefore niche- and antibiotic-specific, with a significantly higher reduction in the extracellular bacterial volume vs IBC volume, and a significantly higher reduction in IBC volume with treatment with Fosfomycin vs. ampicillin (Figure 4K). However, elimination of bacteria within IBCs was highly heterogenous, and regrowth localized to IBCs was observed even in fosfomycin treated chips (Fig. 4 – figure supplement 1A5, B5). Another consequence of this differential clearance was that after the second round of antibiotic treatment, regrowth was observed in only a very small fraction of non-IBC UPEC (Figure 3-Figure supplement 1C). Protection of bacteria within IBCs

therefore has a direct outcome of enabling the reseeding of infection at other locations within the epithelial monolayer.

Lastly, we sought to determine if the bladder duty cycle altered the dynamics of UPEC infection. A comparison between infected bladder-chips with and without the duty cycle (Figure 4L-N, Figure 4-figure supplement 3) revealed a significant increase in the bacterial burden when the duty cycle was implemented (Figure 4N). These results suggest that the bladder filling and voiding cycle influence the uptake and proliferation of UPEC, possibly through physiological changes in the epithelial cells in response to applied strains (Apodaca, 2004; Carattino et al., 2013; Truschel et al., 2002; Wang et al., 2005). In turn, they suggest a deeper connection between the physiology of mechanically active organs such as the bladder and the processes of infection, which can be characterized in detail using this bladder-chip model.

Discussion

In our human bladder-chip model, we recapitulate key aspects of bladder physiology relevant to the study of the earliest stages of UPEC infection and IBC formation. Therefore, superficial bladder epithelial cells, the first cell-type usually infected by UPEC, were cultured both under flow in diluted pooled urine and in co-culture with bladder microvascular endothelial cells. The ability to apply a cyclic mechanical stretch to the PDMS membrane, originally designed to mimic the breathing motion in the lung (Huh et al., 2010b) or the peristaltic motion in the gut (Kim and Ingber, 2013), has been adapted here to mimic the slow expansion and rapid contraction of the micturition cycle. We demonstrate the ability to perform multiple duty cycles while simultaneously imaging the infected device via long-term time-lapse imaging, a technical

advance that is difficult to achieve with bladder explants (Justice et al., 2004) or other *in vitro* studies of UPEC infection of bladder epithelial cells (Andersen et al., 2012; Horsley et al., 2018; Iosifidis and Duggin, 2020; Smith et al., 2006). Using this approach, we found that the total bacterial burden inside infected bladder-chips was significantly higher at a late stage of infection if a duty cycle was applied, unlike the non-significant influence of cyclic stretching on Shigella infection of intestinal-chips under flow conditions (Grassart et al., 2019). The exact mechanisms underlying this phenomenon remain to be explored, but there is an increasing understanding of the role of mechanical forces in regulating innate immune function (Solis et al., 2019). Our results showcase the ability of the bladder-chip model to capture these interactions between mechanical function, physiology, and infection, unlike other infection models reported thus far. A primary focus of *in vitro* models developed so far has been to probe specific aspects of UPEC infection, such as the role of the stratified bladder architecture (Horsley et al., 2018) or the effects of micturition on IBC formation (Andersen et al., 2012; Iosifidis and Duggin, 2020). However, the migration of immune cells into the bladder is difficult to reproduce in these models, and in many of these systems, live-cell imaging remains technically challenging (Horsley et al., 2018; Smith et al., 2006). Furthermore, the models do now allow mechanical manipulations of the cellular co-culture. In that sense, the bladder-chip model complements these existing approaches by providing these additional functionalities. Further development, potentially through the combination of organoid and organ-on-chip approaches, could lead to the development of a fully stratified uroepithelium on-chip.

Neutrophils are the first responders to UPEC infection (Abraham and Miao, 2015; Haraoka et al., 1999), and neutrophil migration involves a series of steps that commences with attachment to the

endothelium under flow, migration on the endothelial surface, diapedesis across the epithelial-
endothelial cell barrier and movement towards the site of infection (Ley et al., 2007; Nourshargh
et al., 2010). Human neutrophils in the bladder-chip model recapitulate all these phenotypes and
perform rapid diapedesis to sites of infection. On the epithelial side, neutrophils formed swarm-
like aggregates, some of which generated myeloperoxidase and neutrophil elastase positive NET-
like structures that extend across many tens of microns (Metzler et al., 2011; Papayannopoulos et
al., 2010), indicative of potent anti-microbial activity. However, neutrophil control of infection
on-chip is partial; this is possibly due to the unrestricted growth of large numbers of extracellular
bacteria and in some instances, exacerbated by the loss of some neutrophils due to flow in the
epithelial channel. Another contributing factor could potentially be the architecture of the PDMS
membrane, which permits neutrophil diapedesis only at fixed spatial locations on-chip.
Neutrophil migration may also be impacted by the relative stiffness of the PDMS membrane.
Nevertheless, the demonstration of NET formation is consistent with the occurrence of these
structures both in the mouse model (Ermer et al., 2009) as well as in the urine of infected
patients (Yu et al., 2017) and suggests that the model is able to recapitulate important aspects of
disease. It is also an important advance for the use of organ-on-chip approaches to recapitulate
NET formation in infectious diseases.

IBCs form immediately after infection and prior to upon neutrophil administration. However,
identification of IBCs architectures with a high degree of confidence was only possible after an
initial treatment with a high dose of antibiotic that eliminated extracellular planktonic bacteria
and improved the optical imaging of bacteria attached to or within epithelial cells. This
methodology enabled us to capture the full cycle of IBC growth from few bacteria to a large

biofilm and subsequent release via shedding and filamentation. Importantly, the compact nature of the device allowed us to image multiple IBCs concurrently on the same chip with a high temporal resolution while simultaneously mimicking the bladder filling and voiding cycles, which is difficult to achieve in bladder explants (Justice et al., 2004) or bladder monoculture *in vitro* model systems (Andersen et al., 2012; Iosifidis and Duggin, 2020). Our observations reiterate the highly dynamic nature of these structures; growth was asynchronous and heterogenous and outcomes included bacterial shedding, exfoliation and filamentation (Hunstad and Justice, 2010; Justice et al., 2004; Scott et al., 2015). Notably, shedding and exfoliation were not mutually exclusive for the time-period of our observations – we report examples of IBCs that shed bacteria and contract in volume before exfoliation.

While IBCs are clearly acknowledged as critical players in early infection, the contribution towards promoting persistence is not completely understood. For example, Blango *et al.*, (Blango and Mulvey, 2010) showed that incubation of bladder explants containing IBCs with a high dose of antibiotics for a period of 18 hours resulted in a substantial sterilization of these structures and concluded that other populations, notably quiescent reservoirs (Mysorekar and Hultgren, 2006) might play a greater role in the establishment of persistent populations. However, the pharmacokinetic profiles of most antibiotics in the host are not time invariant. For example, in the case of ampicillin, a standard regimen of ampicillin treatment is typically a bolus of 250-500 mg of antibiotic administered every 6 hours. Within the serum, ampicillin concentration peaks at a $C_{\max} \sim 3-40 \mu\text{g/ml}$, which is between 1.5 to 20-fold the MIC as measured in human serum (Bryskier, 2020; Putrinš et al., 2015). We therefore chose concentrations that captured these antibiotic exposures (we used ampicillin at 40x MIC measured

in the endothelial cell medium). Ampicillin concentrations in the blood rapidly decay with a half-life of between 60 and 90 minutes with a characteristic pharmacokinetic/pharmacodynamic profile. This period is modelled well by our experimental protocol where phases with high concentration of ampicillin are interspersed with periods with no antibiotic. We are therefore able to model the delivery of two consecutive doses of antibiotic and find that IBCs offer substantial protection against sterilization by a short duration of a high-dose antibiotic treatment and in many instances, bacterial regrowth after two successive rounds of antibiotic administration. Notably, in smaller ‘early IBCs’, bacterial growth continues throughout the period of ampicillin administration, suggesting that the intact nature of the cell membrane likely diminishes the effect of the drug. Although Fosfomycin has a different pharmacokinetic/pharmacodynamic profile it has enhanced cell penetrability. Nevertheless, our results show bacteria in IBCs can regrow following two consecutive 3-hour exposures Fosfomycin at concentrations reported in urine (Bergan, 1990). Together, these results suggest that in UTI infection in patients, IBCs may continue to play a role in reseeding sites of infection for a considerable period after the commencement of antibiotic treatment. This has particularly important implications with regard to the compliance of antibiotic use as proliferating IBCs could rapidly re-seed sites of infection throughout the bladder if antibiotic doses are missed. These unique capabilities of the bladder-chip to realistically model antibiotic treatment regimens for IBCs can be leveraged in the future to screen compounds (Spaulding et al., 2017) and identify optimal antibiotic treatments regimens that can eliminate persistent bacterial populations in IBCs or alter the host-pathogen interaction dynamic in UTIs.

In summary, the bladder-chip model incorporates aspects of bladder physiology highly relevant to early UPEC infection in a platform amenable to long-term live-cell imaging as well as for the administration of antibiotics and therapeutics in a physiologically relevant manner. Our results establish the suitability of this model for immunological and drug-delivery studies and show that IBCs are highly dynamic structures that offer substantial protection from antibiotic clearance for an extended period of time.

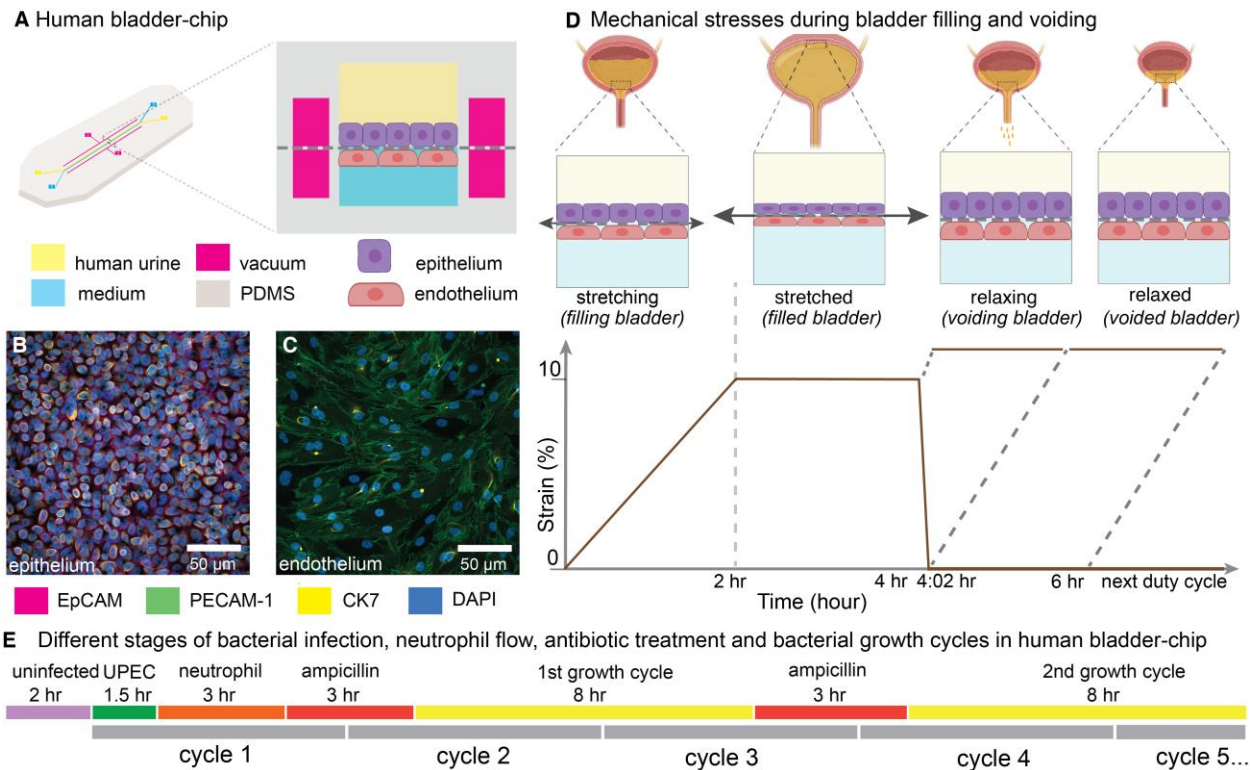


Figure 1: Human Bladder-chip model of UTI recapitulates the physiology of bladder filling and voiding.

(A) Schematic of the human bladder-chip with co-culture of the 5637 human bladder epithelial cell line (epithelium, top) and primary human bladder microvascular endothelial cells (endothelial, bottom) on either side of the stretchable and porous membrane. Pooled human urine diluted in PBS and endothelial cell medium were perfused in the apical and vascular channels respectively to mimic bladder physiology. A negative pressure in the ‘vacuum’ channels (magenta) on either side of the main channel was applied to stretch the porous membrane to mimic stretching of the bladder. (B, C) Immunofluorescence staining of confluent epithelial and endothelial cell monolayers (anti-EpCAM (magenta) and anti-CK7 (yellow) for the epithelial cells and anti-PECAM-1 (green) for the endothelial cells) in an uninfected control chip. Some endothelial cells also stained positive for CK7. Cell nuclei were labeled with DAPI (azure). (D) Schematic of the reconstitution of the bladder filling and voiding cycle via stretching of the membrane with a duty cycle of 6 hours. The cycle consisted of a linear increase in strain through

584 stretching of the membrane (*filling bladder*, 0 to 2 hours), maintenance of the membrane under
585 stretch (*filled bladder*, 2 to 4 hours), a quick relaxation of applied strain over 2 minutes (*voiding*
586 *bladder*, 4:02 hours) and maintenance without applied strain (*voided bladder*, 4:02 hours to
587 6hours). (E) An overview of the timeline of the experimental protocol including infection,
588 addition of neutrophils via the vascular channel, and two cycles of antibiotic treatment
589 interspersed by two bacterial growth cycles. The consecutive bladder duty cycles are indicated.
590

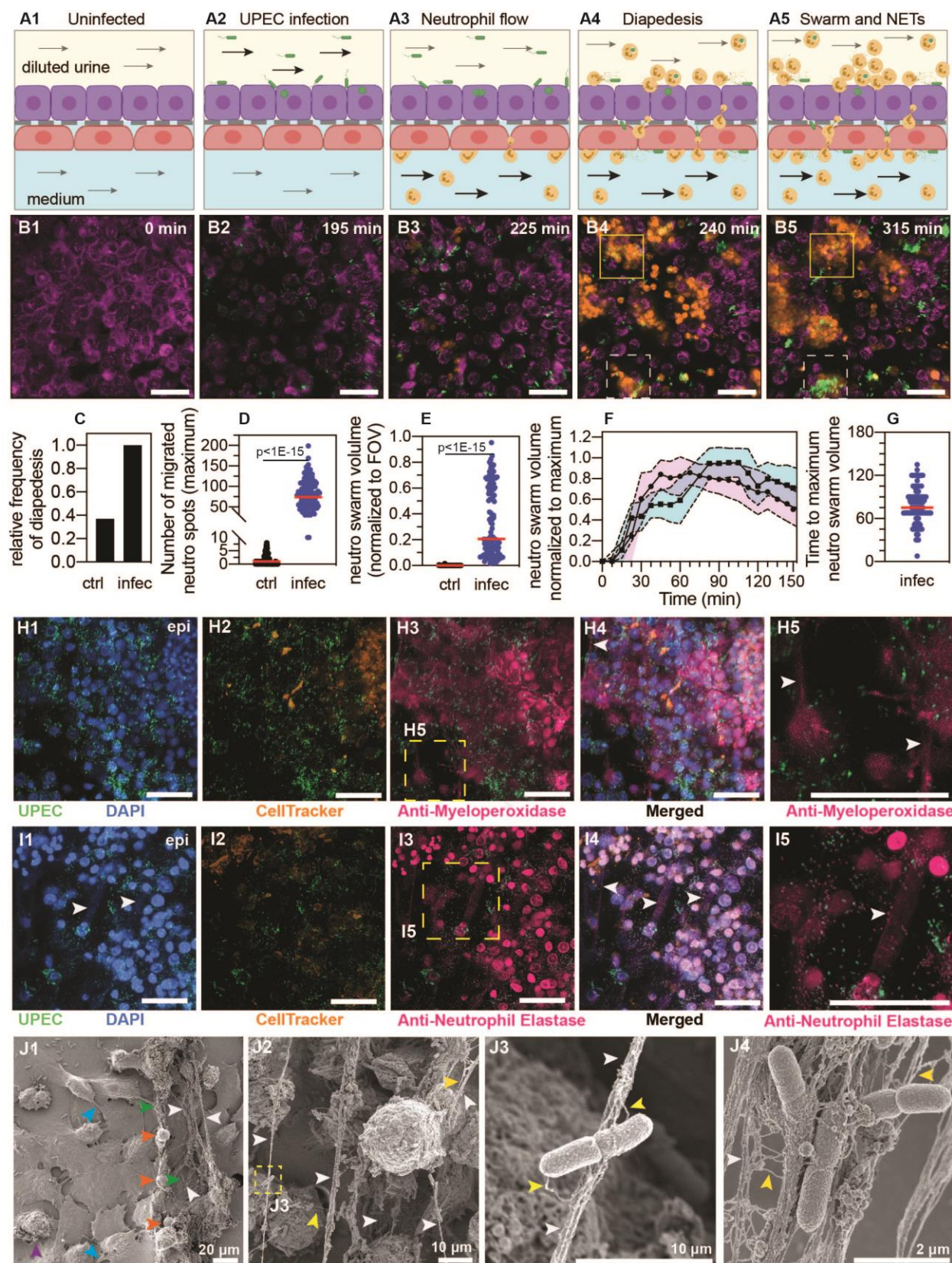


Figure 2: Neutrophil diapedesis and NET formation on-chip.

(A1-A5) Schematic of the UPEC infection, introduction of neutrophils and diapedesis of neutrophils across the epithelial-endothelial barrier to sites of infection. Flow in the epithelial and endothelial channels is indicated by arrows; the flow rate was increased upon introduction of neutrophils in the vascular channel to increase attachment. Increased flow rate in the epithelial and endothelial channel is indicated by black arrows. (B1-B5) Snapshots from time-lapse imaging highlighting each stage in the infection cycle shown in (A1-A5). Bladder epithelial cells (magenta) and neutrophils (amber) were identified with membrane (Cell Mask Orange) and cytoplasmic (Cell Tracker Deep Red) dyes, respectively. UPEC identified via constitutive expression of YFP are shown in green. Neutrophil swarms could either control bacterial growth (yellow dashed square, compare B4 vs B5) or did not manage to restrict bacterial growth (white dashed square, compare B4 vs B5). (C) Bar charts for relative frequency of neutrophil diapedesis (black) in n=3 uninfected control bladder-chips and n=4 infected bladder-chips. Data obtained from n=95 and n=116 fields of view, each of which was $206 \times 206 \mu\text{m}^2$. (D) Quantification of the number of neutrophils detected on the epithelial layer, in control and infected bladder-chips. The red bar represents the median value, $p < 1\text{E-}15$. In many instances in the uninfected control bladder-chips, no neutrophil diapedesis is detected. Data obtained from n=95 and n=130 fields of view, each of which was $206 \times 206 \mu\text{m}^2$. (E) A plot of the maximum neutrophil swarm volume on the epithelial layer normalized to the total volume for n=67 and n=118 fields of view on n=3 uninfected control and n=3 infected bladder-chips. The red bar represents the median value. $p < 1\text{E-}15$. (F) A plot of neutrophil swarm volume on the epithelial layer over time for n=51 and n=40 fields of view for n=2 technical replicates indicated by squares and circles. For each time profile, the volume is normalized to the maximum volume attained over the timeseries and t=0 refers to the timepoint at which neutrophils are introduced into the vascular channel (G) Plot of

617 the time to reach the maximum swarm volume in n=154 fields of view across n=4 infected
618 bladder-chips. (**H1-H5, I1-I5**) NET formation by neutrophils on the epithelial layer. The
619 neutrophils are identified by a cytoplasmic dye (CellTracker Deep Red, false coloured in amber)
620 (**H2, I2**) and immunostaining with an anti-myeloperoxidase antibody (**H3**, zooms in **H5**) or an
621 anti-neutrophil elastase antibody (**I3**, zooms in **I5**). Merged images in each case are shown in **H4**
622 and **I4**. UPEC identified via YFP expression is shown in spring green. Nuclear labelling with
623 DAPI is shown in azure. (**H5**) NETs, identified via anti-myeloperoxidase staining or anti-elastase
624 staining are indicated with white arrows in (**H5**) and (**I5**) respectively. (**J1-J4**) Scanning electron
625 micrographs of the epithelial layer of an infected bladder-chip 2 hours after the introduction of
626 neutrophils in the endothelial channel. (**J1**) Neutrophils (amber arrowheads) are visible above a
627 layer of epithelial cells. Thick bundles consisting of many thinner NET structures between
628 neutrophils are indicated by white arrowheads, and examples of individual UPEC bacteria within
629 the NETs are indicated by green arrowheads. A heavily infected epithelial cell with UPEC
630 visible on the epithelial cell (purple arrowhead), and appendages between epithelial cells (cyan
631 arrowheads) are also visible. (**J2**) Micrographs showing thick bundles consisting of many thinner
632 NET structures (white arrowheads) that extend between cells and trap many individual bacteria.
633 Thinner NET fibers (yellow arrowheads) are also visible. (**J3**) Zooms of the regions in **J2**
634 identified by a yellow dashed square. Two bacteria held by a thick bundle composed of many
635 thinner NET fibers are shown. (**J4**) Micrograph highlighting multiple bacteria trapped between
636 NET bundles. p-values in **D** and **E** were calculated using a Mann-Whitney test. Scale bar = 50
637 μm in **B1-B5, H1-H5, I1-I5**.

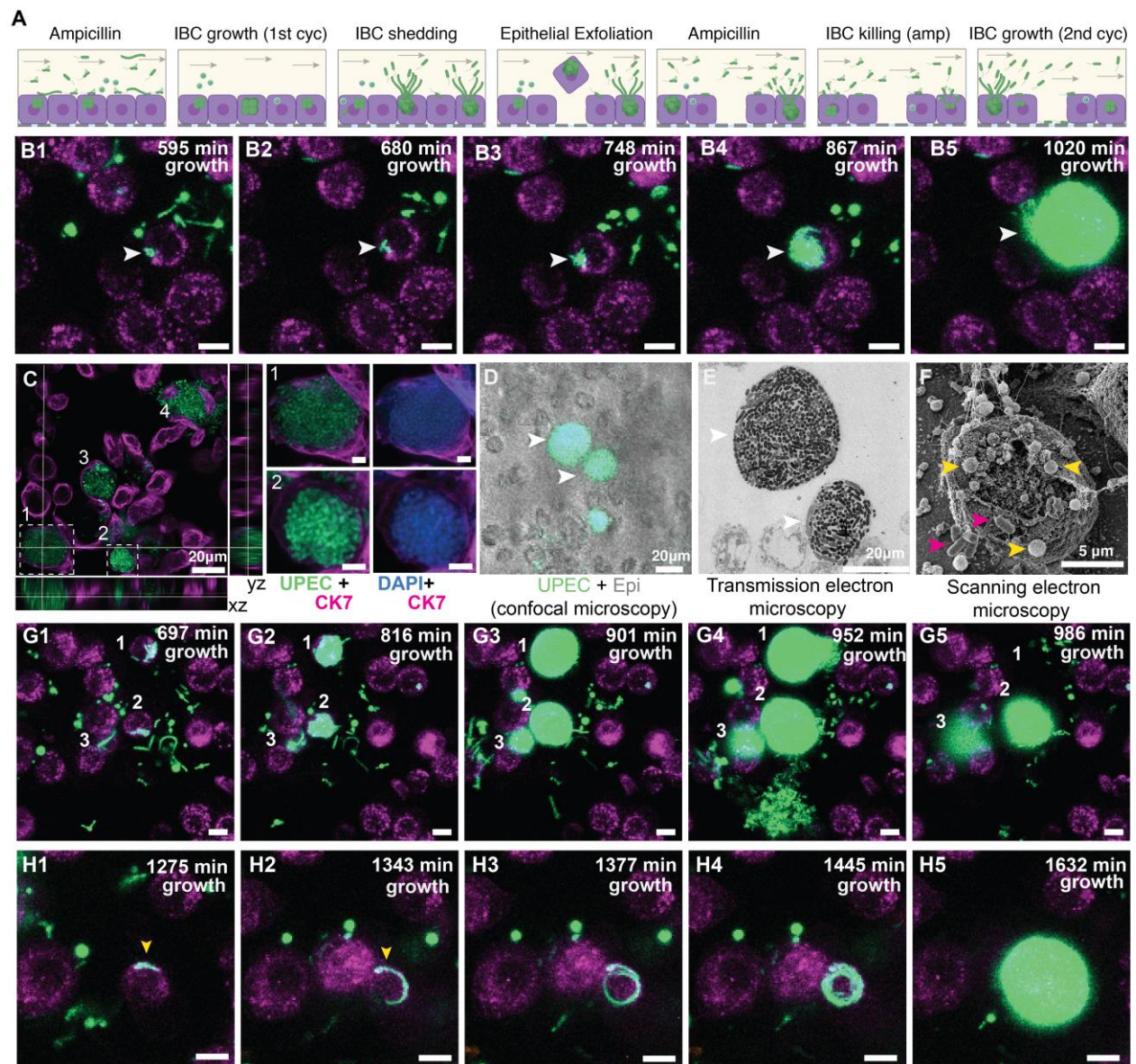


Figure 3: Bladder-chip reveals dynamics of IBC growth, shedding and exfoliation.

(A) Schematics of the host-pathogen interactions within IBCs between successive rounds of antibiotic treatment with outcomes including shedding of bacteria and cell exfoliation shown. Arrows indicate the flow of diluted urine in the epithelial channel. (B1-B5) Timeseries for the growth of an IBC from few bacteria (white arrowhead) after the first round of ampicillin treatment. Bacteria grow to completely fill the cell volume (B5). (C) Immunofluorescence characterization of two IBCs; the intracellular nature of growth is confirmed with staining with an anti-CK7 antibody. Correlative light (D) and transmission electron micrographs (E) show two

IBCs filled with both rod-shaped and coccoid-shaped bacteria. **(F)** Coccoid-shaped bacteria (yellow arrowheads) and rod-shaped bacteria (magenta arrowheads) are also visible in a scanning electron micrograph of an infected epithelial cell. IBCs on infected bladder-chips shown in **C-F** were fixed ca. 13.5 hours after UPEC infection and 6 hours into the first growth cycle. **(G1-G5)** Three examples of IBC growth, labelled 1 – 3 with differing outcomes. Unrestricted bacterial growth is observed within all IBCs. In IBC#1 at timepoint **(G4)** the IBC begins to shed bacteria into the surrounding medium. The cell exfoliates in the time interval between **(G4 and G5)**. In IBC#2, bacterial shedding is visible at **(G4)**, and shedding continues until end of the timeseries with a reduction in bacterial volume. In contrast, growth within IBC#3 is slower and neither shedding nor exfoliation occurs within the timeseries. **(H1-H5)** Timeseries highlighting an example of filamentous UPEC growth within an IBC. Scale bars, 10 μm in **B1-B5, G1-G5 and H1-H5**.

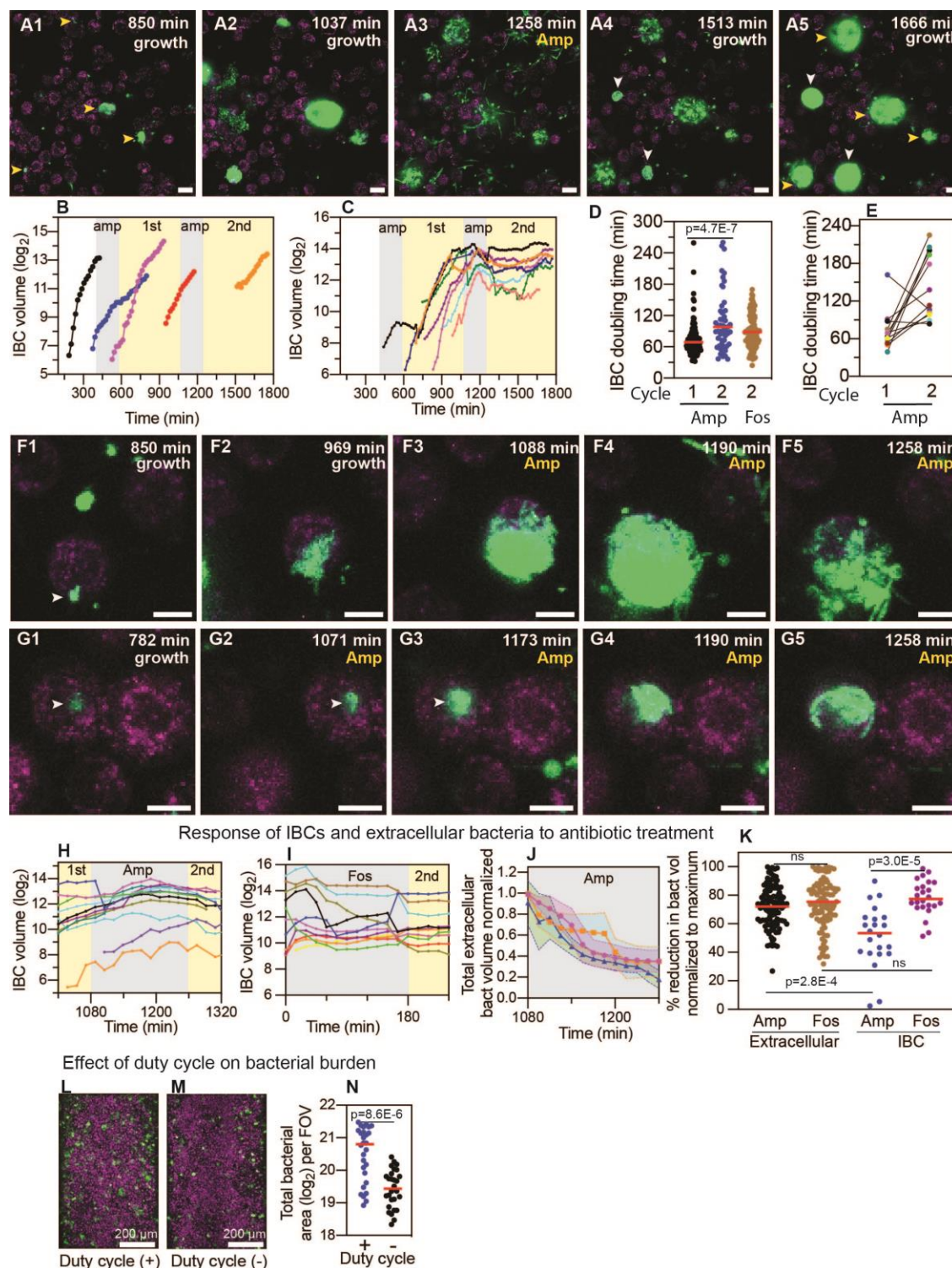


Figure 4: IBCs offer a semi-protective niche that delays clearance of bacteria by antibiotics. (A1-A5) Bacteria persist and grow in IBCs despite antibiotic treatment. Snapshots show the growth of four IBCs with variable growth rates (A1-A2). Ampicillin treatment eliminates some

664 but not all of the bacteria within each IBC (**A3**). Growth resumes at all sites in (**A4**, **A5**),
665 formation of new IBCs in the second growth cycle is indicated by white arrowheads. (**B**) Plots of
666 logarithm of bacterial volume within five separate IBCs demonstrates exponential bacterial
667 growth. IBCs are seeded dynamically; growth can occur either in the first or second growth
668 cycle, or prior to the administration of antibiotic, or in few cases continues in the presence of the
669 antibiotic. (**C**) Plots of the logarithm of bacterial volume vs. time for n=8 IBCs tracked across
670 two growth phases with an intermediate period of ampicillin treatment. In the growth phases,
671 growth is exponential and bacterial volume continues to increase for up to ca. 120 minutes after
672 administration of antibiotic before declining due to loss of bacteria. In each case, growth resumes
673 after the antibiotic is removed. (**D**) Scatter plots of the doubling time of bacterial volume in IBCs
674 as measured in the first growth cycle (n=102) and the second growth cycle (n=59) from n= 3
675 bladder-chips. Growth in the second cycle is significantly slower ($p=4.7E-7$), red line represents
676 the median value. (**E**) Doubling time of bacterial volume in IBCs in the first and second growth
677 cycle for some of the IBCs in (**D**) that survived the antibiotic treatment. In n=16 out of 18
678 instances, growth is slower in the second growth cycle. (**F1-F5**) High resolution time-series that
679 highlights bacterial growth within an IBC prior to (**F1**, **F2**) and after (**F3-F5**) administration of
680 ampicillin. Some bacteria within this IBC are subsequently eliminated (**F5**). (**G1-G5**) High
681 resolution time-series that highlights bacterial growth within an IBC prior to (**G1**, **G2**) and after
682 (**G3-G5**) administration of ampicillin. The bacterial volume within this IBC is not diminished by
683 antibiotic treatment (**G5**). (**H**) Plots of logarithm of bacterial volume within n=11 IBCs before,
684 during, and after the second round of ampicillin treatment. (**I**) Plots of logarithm of bacterial
685 volume within n=9 IBCs before, during, and after the second round of fosfomycin treatment. (**J**)
686 Plot of the volume of extracellular bacteria upon antibiotic administration from n=103 fields of

view, each of which was $206 \times 206 \mu\text{m}^2$ in size, from $n=3$ bladder-chips. The bacterial volumes are normalized to the volume immediately prior to the antibiotic administration. (**K**) Scatter plot of the extracellular bacterial volume ($n=105$) and bacterial volume within IBCs ($n=22$) from $n=3$ bladder-chips after ampicillin treatment and extracellular bacterial volume ($n=101$) and bacterial volume within IBCs ($n=23$) from $n=1$ bladder-chip after fosfomycin treatment as a fraction of the maximum bacterial volume prior to antibiotic treatment. Red line represents the median value, $p=2.8\text{E-}4$ (extracellular amp vs IBC amp), $p=3.0\text{E-}5$ (IBC amp vs IBC fosfomycin) calculated using Kruskal-Wallis ANOVA Test, 'ns' represents $p>0.05$ (**L, M**) Representative images from the epithelial face of the infected bladder-chips with or without duty cycle, fixed at ca. 13.5 hours after UPEC infection and 6 hours into the first growth cycle. (**N**) Scatter plots of the logarithm of the total bacterial area across $n=14$ fields of view from infected bladder-chips with ($n=2$) and without ($n=2$) the application of the duty cycle, $p=8.6\text{E-}6$. p -values calculated using a Mann-Whitney test. Yellow rectangular area in **B, C, H** and **I** represent the 1st and 2nd growth cycles. Grey rectangular area in **B, C, H, I** and **J** represent the rounds of ampicillin treatment. Scale bars, $10 \mu\text{m}$ in panels **A1-A5, F1-F5**, and **G1-G5**.

Cell type	Cell density/ $10^4 \mu\text{m}^2$
Epithelial	31.7 ± 5.1
Endothelial	4.0 ± 0.6

Table 1.

Characterization of epithelial and endothelial cell densities from a total of n=18 fields of view in both the epithelial and endothelial layers from n=2 bladder-chips.

Figure Supplement Legends

Figure 1-figure supplement 1: Characterization of co-cultures of bladder epithelial cells and bladder endothelial cells in bladder-chip.

Immunofluorescence characterization of 5637 bladder epithelial cells in bladder-chip for Epithelial Cell Adhesion Molecule (EpCAM) (A), cytokeratin 7 (CK7) (B), and cytokeratin 8 (CK8), a marker for differentiated uroepithelial cells (F). Immunofluorescence characterization of primary human bladder microvascular endothelial cells in bladder-chip for tight junction markers such as Platelet Endothelial Cell Adhesion Molecule-1 (PECAM-1) (C) and vascular endothelial cadherin (VE-cadherin) (G). Some endothelial cells also express CK7 (D). Filamentous actin staining for epithelial (E) and endothelial (H) cells. Cell nuclei were labeled with DAPI (azure) in all panels. Scale bars, 50 μm in all panels.

Figure 1-figure supplement 2: Characterization of monocultures of 5637 bladder epithelial cells and HMVEC-Bd bladder microvascular endothelial cells.

Characterization of the 5637 bladder epithelial cells for epithelial tight junction markers such as Epithelial Cell Adhesion Molecule (EpCAM) (A), epithelial cadherins (E-cadherin) (B), Zonula Occludens-1 (ZO-1) (C), and filamentous actin (Phalloidin) (D). Bladder endothelial cells express tight junction markers such as vascular, Platelet Endothelial Cell Adhesion Molecule-1 (PECAM-1) (E), endothelial cadherin (VE-cadherin) (F) and filamentous actin (Phalloidin) (G). Some endothelial cells also showed staining for CK7 (H). Characterization of the 5637 cells for the uroepithelial cell marker cytokeratin 7 (CK7) (I), for umbrella cell specific markers cytokeratin 8 (CK8) (J) and uroplakin 3a (Up3a) (K), and the basal cell marker cytokeratin 1 (CK1) (L). CK1 expression was sparse and lower than CK7 and CK8, data obtained from 2 fields of view in an ibidi μ -Slide 8 well (M). Red lines represent the median value. Epithelial and endothelial cells were grown to ca. 75-90% confluence in ibidi 8-wells. Cell nuclei were labeled with DAPI (cyan). (N) Characterization of primary bladder epithelial cells for CK8 expression. Cell nuclei were labeled with DAPI (cyan). Scale bars, 10 μm in (A-L, N). Scale bars, 10 μm in (A-L, N).

Figure 1-figure supplement 3: Quantification of the linear strain in the PDMS membrane as a function of applied negative pressure in the vacuum channels of the bladder-chip.

Pore-to-pore distance was measured in the PDMS membrane (n=14) on human bladder chip under different values of applied pressure and used to calculate the linear strain ($\Delta l = \frac{l_s - l_r}{l_r}$). l_s and l_r refer to the pore-to-pore distance in the stretched (l_s) and relaxed state (l_r).

Figure 2-figure supplement 1: Quantification of UPEC attachment to bladder epithelial cells on-chip under flow.

Ratio of number of attached UPEC to the average number of epithelial cells in n=25 (magenta line), n=38 (orange line) and n=34 (blue line) fields of view, each 206 x 206 μm^2 across on the epithelial layer of n=3 infected bladder-chips. In each case, the protocol results in less than 1 focus of infection per epithelial cell at the end of the 90-minute infection period. The dotted lines and the shaded regions represent the standard deviation.

Figure 2-figure supplement 2: Timeseries highlighting neutrophil diapedesis and swarm formation.

Additional images that highlight the diapedesis of neutrophils across the epithelial-endothelial barrier and the formation of neutrophil swarms. Bladder epithelial cells (magenta) and neutrophils (amber) were identified with membrane (Cell Mask Orange) and cytoplasmic (Cell Tracker Deep Red) dyes, respectively. UPEC identified via constitutive expression of YFP are shown in green. In all images, scale bar = 50 μm .

Figure 2-figure supplement 3: Neutrophils isolated from human blood are CD15+.

Images of neutrophils isolated via negative depletion from human blood and labelled with a cytoplasmic dye (Cell Tracker Deep Red) (A) and immunostained with an anti-CD15 antibody (B). (C) Merged image for both channels confirms that all neutrophils are CD15+.

Figure 2-figure supplement 4: Neutrophil attachment to endothelial cells is enhanced upon bacterial infection.

Fluorescent (A) and brightfield (B) imaging of the endothelial layer of an uninfected bladder-chip. The few neutrophils (identified by CellTracker Deep Red, amber) attached to the endothelial layer are indicated by white arrowheads. Fluorescent (C) and brightfield (D) imaging of the endothelial layer of an infected bladder-chip, 1.5 hours after infection of the epithelial layer. Neutrophils attached to the endothelial layer are marked by white arrowheads and examples of diapedesis through the PDMS pores to the epithelial layer are marked with magenta arrowheads. In all panels, neutrophils (amber) were introduced into the vascular channel of the bladder-chip under a flow rate of 3 ml/hour corresponding to a shear stress $\eta=1$ dyne/cm².

Figure 2-figure supplement 5: Neutrophil diapedesis is stimulated by a pro-inflammatory cytokine gradient across the epithelial-endothelial barrier.

(A) Representative images of the epithelial layer of an uninfected control bladder-chip, 2 hours after the introduction of neutrophils in the endothelial channel. No neutrophil diapedesis is observed. (B) Representative image of the epithelial layer of an uninfected control bladder-chip exposed to a cocktail of pro-inflammatory cytokines (Interleukin-1 α , Interleukin-1 β , Interleukin-6 and Interleukin-8, each at 100 ng/ml) added to the diluted urine on the epithelial side and maintained under flow for 2 hours. Epithelial cells (magenta, identified via CellMask Orange) and neutrophils (amber, identified via CellTracker Deep Red) are shown. (C) Representative image of the epithelial layer of an infected bladder-chip 2 hours after the introduction of neutrophils in the endothelial channel. UPEC identified via constitutive expression of YFP are shown in green. (D) Scatterplot of maximum number of neutrophils detected in 206 x 206 μm^2 fields of view under control (n= 26), cytokine stimulation (n=26) and infection (n=130). P-values were calculated using Kruskal-Wallis ANOVA Test. Red lines represent median values. Scale bars, 50 μm .

Figure 2-figure supplement 6: NETs formation on the epithelial and endothelial layers of an infected bladder-chip.

(A1-A3) Additional example of NETs formation by neutrophils on the epithelial layer (epi) of an infected bladder-chip. Neutrophils are identified via immunostaining with an anti-myeloperoxidase antibody (A1-A2). UPEC identified via YFP expression are shown in spring green (A1). Nuclear labelling with DAPI is shown in azure (A2). A merged image is shown in A3. (B1-B3) An example of NETs formation by neutrophils on the endothelial layer (endo) of an infected bladder-chip. UPEC identified via YFP expression are shown in spring green and

nuclear labelling with DAPI is shown in azure (**B1**). Neutrophils are identified via immunostaining with an anti-neutrophil elastase antibody (**B2**). A zoomed image corresponding to the white dashed box in **B2** is shown in **B3**. In all images, scale bar = 50 μ m.

Figure 2-figure supplement 7: SEM characterization of uninfected and infected bladder-chips.

(**A**) SEM image of the confluent epithelial layer of an uninfected bladder-chip. Appendages between epithelial cells are indicated by cyan arrowheads. (**B**) Example from an infected bladder-chip without the addition of neutrophils. Long filaments characteristic of NET formation is not observed. Individual UPEC on the surface of the epithelial cells are indicated by green arrowheads. Appendage between epithelial cells is indicated by a cyan arrowhead (**C**) Additional example of formation of NETs by a large swarm of neutrophils on the epithelial layer of an infected bladder-chip. NETs are indicated by white arrowheads, and large clusters of neutrophils are indicated by dashed amber circles.

Figure 2-figure supplement 8: Neutrophils do not form NETs in response to shear stress in the bladder-chip.

Neutrophils infused through the vascular channel of an infected bladder-chip were collected and characterized via immunofluorescence for myeloperoxidase (**A-C**) and neutrophil elastase expression (**D-F**) to identify the formation of NETs, indicated by dotted white circles. All neutrophils are labelled by the cytoplasmic CellTracker dye (shown in amber in **B**, **E**). Both myeloperoxidase expression (marked with dotted white circles in **C**) and elastase expression (marked with dotted white circles in **F**) coincide with infected neutrophils (**A**, **D**). UPEC are identified via YFP expression and colored spring green, nuclear labelling is indicated in azure. Scale bars, 50 μ m in all panels.

Figure 3-figure supplement 1: Non growing UPEC in response to ampicillin administration in the bladder-chip.

(**A**) Measurement of ampicillin minimum inhibitory concentration (MIC) in endothelial cell medium for the UPEC strain used in these experiments. (**B1-B5**) Example of a non-growing clump of UPEC within an epithelial cell following the first growth cycle (indicated by white arrowheads in all images). The bacteria are non-growing throughout the first growth cycle (**B1**, **B2**), the second cycle of ampicillin treatment (**B3**) and subsequently after the removal of antibiotic (**B4**, **B5**). (**C**) Classification of the growth state of UPEC as growing (black) or non-growing (white) across n=108 fields of view in total from n=3 infected bladder chips during the first and second growth periods. (**D**) Scatter plot for the distribution of lag time (measured as the time taken to resume growth after removal of antibiotic) for intracellular bacterial microcolonies during the first (n=133) and second (n=16) growth cycles. Red line represents the median value. Scale bars, 10 μ m in **B1-B5**. (**E**) Orthogonal section view and (**F**) maximum intensity projection of an IBC formation after fosfomycin treatment of a chip reconstituted with 5637 cells. (**G**) Maximum intensity projection and zooms (**H**, **I**) of IBCs formed subsequent to Fosfomycin treatment in primary bladder epithelial cells.

Figure 3-figure supplement 2: Immunofluorescence characterization of IBC formation.

(**A**) Confocal images of two IBCs within epithelial cells with different morphologies. UPEC are labelled in spring green, anti-CK8 staining is shown in magenta, F-actin labelling is shown in

yellow, and nuclear labelling with DAPI is shown in azure. IBCs on the infected bladder chip were fixed ca. 13.5 hours after UPEC infection and 6 hours into the 1st growth cycle.

Figure 3-figure supplement 3: IBC formation from filamentous UPEC.

(A1-A5) Additional example of intracellular growth of filamentous UPEC that develops into an IBC. The growing filament (A1-A2) is eventually restricted by the cellular volume and bends (A3) before reductive division (marked by white arrowhead in A3) and IBC formation occurs. Scale bars, 10 μ m in A1-A5.

Figure 4-figure supplement 1: UPEC regrowth on-chip despite two consecutive periods of fosfomycin treatment.

(A, B) Examples of UPEC growth in infected bladder chips reconstituted with primary epithelial cells. Regrowth and IBC formation after two rounds of antibiotic treatment are observable in A5, B5. (C) Growth statistics for IBCs in chips reconstituted with 5637 cells after the two periods of fosfomycin treatment.

Figure 4-figure supplement 2: UPEC growth in IBCs during ampicillin treatment

(A1-A5) Additional examples of UPEC growth during ampicillin treatment. (A1) Two IBCs (marked 1 and 2) at the start of ampicillin treatment. The IBC marked 1 exfoliates (A2) whereas the remaining IBC-2 continues to grow (A1-A3). Towards the end of this period, the bacteria filament (A4) before clearance due to the antibiotic is observed (A5). (B1-B5) High resolution time-series that highlights bacterial growth within an IBC prior to (B1) and during (B2-B5) administration of ampicillin. The bacterial volume within this IBC is not diminished by antibiotic treatment (B5). Scale bars, 10 μ m in all the panels.

Figure 4-figure supplement 3: UPEC infection leads to a higher bacterial burden in bladder-chips perturbed with duty cycle.

Additional examples of UPEC growth in infected bladder chips with (A) and without (B) duty cycle.

Video Legends

Figure 2-video 1

File Name: **Figure 2-video 1**, Description: Infection of bladder-chip with UPEC, diapedesis of neutrophils across the epithelial-endothelial barrier and formation of swarms ([Figure 2B1-B5](#)).

Stage 1: Prior to infection, the uninfected cells of the epithelial layer (magenta) are imaged (0-120 mins).

Stage 2: UPEC (green) are introduced into the epithelial channel via flow and infection proceeds under flow for 120-210 min.

Stage 3: Neutrophils (amber) are introduced into the vascular channel of the infected bladder-chip via flow (210 min onwards).

Stage 4: Neutrophils undergo diapedesis within 15-30 minutes and are visible on the epithelial side (210-240 min). UPEC can be seen internalized by neutrophils.

Stage 5: Neutrophils aggregate and form a neutrophil swarm (240 min onwards) on the epithelial side.

Figure 2-video 2

File Name: **Figure 2-video 2**, Description: Neutrophil diapedesis and swarm formation on the epithelial side of UPEC infection ([Figure 2-figure supplement 2A1-A5](#)).

Stage 1: Prior to infection, the uninfected cells of the epithelial layer (magenta) are imaged (0-120 mins).

Stage 2: UPEC (green) are introduced into the epithelial channel via flow and infection proceeds under flow for 120-210 min.

Stage 3: Neutrophils (amber) are introduced into the vascular channel of the infected bladder-chip via flow (210 min onwards).

Stage 4: Neutrophils undergo diapedesis within 15 minutes and are visible on the epithelial side (210-240 min). UPEC can be seen internalized by neutrophils.

Stage 5: Neutrophils aggregate and form a neutrophil swarm (240 min onwards) on the epithelial side.

Figure 3-video 1

File Name: **Figure 3-video 1**, Description: Formation of intracellular bacterial community inside epithelial cell arising from few bacteria ([Figure 3B1-B5](#)).

An intracellular bacterial community is seeded inside a bladder epithelial cell (magenta, stained with Cell Mask Orange) by few UPEC (green) to form an intracellular bacterial community during the first growth cycle (578-1054 min, ca. 8 hr.). During subsequent ampicillin treatment (1071-1258 min, ca. 3 hr.), the IBC shed bacteria and eventually exfoliated from the epithelial layer.

Figure 3-video 2

File Name: **Figure 3-video 2**, Description: IBC shedding and exfoliation ([Figure 3G1-G5](#)).

UPEC (green) divide and proliferate intracellularly in three epithelial cells (magenta, stained with Cell Mask Orange) to form IBCs. Two late-stage IBCs shed bacteria (ca. 935-969 min). One of these two IBCs subsequently exfoliated (ca. 986 min) whereas the other IBC shrank in volume due to the loss of shed bacteria. The third IBC did not shed bacteria during the first growth cycle (578-1054 min, ca. 8 hr.).

Figure 3-video 3

File Name: **Figure 3-video 3**, Description: Filamentous bacterial growth within an IBC ([Figure 3H1-H5](#)).

Filamentous UPEC (green) grow intracellularly in an epithelial cell (magenta, stained with Cell Mask Orange) to form an IBC during the second growth cycle (1275 min onwards). Shedding of bacteria, some of which appear filamentous was subsequently observed later in the time series (ca. 1649-1768 min).

Figure 3-video 4

File Name: **Figure 3-video 4**, Description: Filamentous bacterial growth within an IBC ([Figure 3-figure supplement 3A1-A5](#)).

Filamentous UPEC (green) grow intracellularly in an epithelial cell (magenta, stained with Cell Mask Orange) to form an IBC during the first growth cycle (578-1054 min, ca. 8 hr.). The IBC eventually exfoliates during the time series.

Figure 4-video 1

File Name: **Figure 4-video 1**, Description: Bacteria within an IBC can persist and grow within an IBC despite the antibiotic treatment ([Figure 4A1-A5](#)).

Proliferation of UPEC (green) within four epithelial cells (magenta, stained with Cell Mask Orange) during the 1st growth cycle (578-1054 min, ca. 8 hr.) leads to the formation of IBCs. The bacteria within the four IBCs persist during the (~40x MIC) ampicillin treatment (1071-1258 min, ca. 3 hr.) In each case, bacterial clearance was observed during the ampicillin treatment, but all four IBCs persisted over the course of the treatment. Bacterial growth subsequently resumed within all four IBCs post ampicillin washout during the second growth cycle (1275 min onwards). Two new IBCs were formed during the second growth cycle (1275 min onwards). IBC fluxing and filamentation could be observed towards the end of time series.

Figure 4-video 2

File Name: **Figure 4-video 2**, Description: Ampicillin mediated bacterial clearance is delayed within an IBC ([Figure 4F1-F5](#)).

Proliferation of UPEC (green) within an epithelial cell (magenta, stained with Cell Mask Orange) during the 1st growth cycle (578-1054 min, ca. 8 hr.) to form an IBC. The bacteria within the IBC persisted during the (~40x MIC) ampicillin treatment (1071-1258 min, ca. 3 hr.). Bacterial proliferation continued during the first two hours of the ampicillin treatment (1071-1190 min, ca. 2 hr.). Bacterial killing was subsequently observed later during the ampicillin treatment (1190-1258, ca. 1 hr.). Some bacteria within the IBC persisted throughout the ampicillin treatment and resumed proliferation during the second growth cycle (1275 min onwards).

Figure 4-video 3

File Name: **Figure 4-video 3**, Description: Ampicillin mediated bacterial clearance is delayed within an IBC ([Figure 4-figure supplement 1A1-A5](#)).

Proliferation of UPEC (green) within two epithelial cells prior to the ampicillin treatment during the 1st growth cycle (578-1054 min, ca. 8 hr.). IBC#1 exfoliates from the epithelial layer (ca. 1105 min). Bacteria within IBC#2 continued to proliferate during the first two hours of the ampicillin treatment (1071-1190 min, ca. 2 hr.). Bacterial clearance was subsequently observed

later during the ampicillin treatment (1190-1258, ca. 1 hr.). IBC#2 eventually exfoliated from the epithelial layer towards the end of the time series (1292 min).

Figure 4-video 4

File Name: **Figure 4-video 4**, Description: Bacteria can continue growing within an IBC for the entire duration of ampicillin treatment ([Figure 4G1-G5](#)).

Proliferation of UPEC (green) within an epithelial cell (magenta, stained with Cell Mask Orange) during the 1st growth cycle (578-1054 min, ca. 8 hr.) to form an IBC. Bacterial growth within the intact IBC continued both during the ampicillin treatment (~40x MIC, 1071-1258 min, ca. 3 hr.) as well as after the ampicillin was washed out during the 2nd growth cycle (1275 min onwards). Eventually, the IBCs shed bacteria (1700-1751 min, ca. 1hr) towards the end of time series.

Figure 4-video 5

File Name: **Figure 4-video 5**, Description: Bacteria can continue growing within an IBC during the ampicillin treatment ([Figure 4-figure supplement 1B1-B5](#)).

Proliferation of UPEC (green) within an epithelial cell (magenta, stained with Cell Mask Orange) during the 1st growth cycle (578-1054 min, ca. 8 hr.) to form an IBC. Bacterial growth within the intact IBC continued both during the ampicillin treatment (~40x MIC, 1071-1258 min, ca. 3 hr) as well as after the ampicillin was washed out during the 2nd growth cycle (1275 min onwards). The late-stage IBC eventually shed bacteria and filamentous bacterial growth (1632-1717 min, ca. 1.5 hr) was also observed towards the end of time series.

987

988 **Acknowledgements**

989 V.V.T gratefully acknowledges support by a Human Frontier Science Program (HFSP) Long-
990 Term Fellowship (LT000231/2016-L) and a European Molecular Biology Organization (EMBO)
991 Long-Term Fellowship (921-2015). This research was supported by a grant awarded to J.D.M by
992 the Swiss National Science Foundation (SNSF) (Project Funding, 310030B_176397) and the
993 National Centre of Competence in Research AntiResist (51NF40_180541), funded by the SNSF.
994 The authors thank the entire team of EPFL Bioimaging & Optics Core Facility for their
995 assistance in confocal live cell imaging and post analysis in Bitplane Imaris. The authors also
996 acknowledge Marie Croisier at the EPFL Biological Electron Microscopy Facility for help in
997 optimizing the protocol for TEM of infected bladder-chip. The authors thank and credit
998 BioRender.com for the illustrations and schematics used in this manuscript.

999

1000 Materials and Methods

Reagent or resource	Designation	Source or reference	Identifiers	Additional information
strain, strain background (Uropathogenic <i>Escherichia coli</i>)	CFT073	PMID: 2182540	NCBI: txid199310	originally isolated from a pyelonephritis patient and provided by Prof. H.L.T. Mobley, University of Michigan, USA
recombinant DNA reagent	pZA32-YFP (plasmid)	PMID: 9092630		(Lutz and Bujard, 1997)
strain, strain background (Uropathogenic <i>Escherichia coli</i>)	CFT073-pZA32-YFP, CFT073	this paper		this study
cell line (<i>Homo sapiens</i>)	HTB-9 TM bladder epithelial cells	ATCC	Cat#:5637	
cell line (<i>Homo sapiens</i>)	HMVEC-Bd – Human Bladder Microvascular Endothelial Cells	Lonza	Cat#:7016	
Biological sample (<i>Homo sapiens</i>)	Human primary bladder epithelial cells	Cell Biologics	Cat#:H-6215	
other	RPMI-1640 medium	ATCC	Cat#:30-2001	
other	Gibco TM RPMI 1640 Medium, no phenol red	Thermofisher	Cat#:11835063	
other	Gibco TM Fetal Bovine Serum, Premium Plus	Thermofisher	Cat#: A4766801	
other	Complete Human Epithelial Cell Medium with growth factor supplement	Cell Biologics	Cat#: H6621	
other	EGM TM -2 MV Microvascular Endothelial Cell Growth Medium-2 BulletKit TM	Lonza	Cat#:CC-3202	
other	EBM-PRF Endothelial Medium Phenol-red free, 500 ml	Lonza	Cat#:CC-3129	
other	EGM TM -2 Endothelial SingleQuots TM Kit	Lonza	Cat#:CC-4176	
other	Gibco TM Antibiotic-Antimycotic (100X)	Thermofisher	Cat#:15240062	
other	Gibco TM Trypsin-EDTA (0.05%), phenol red	Thermofisher	Cat#:25300054	
drug	Chloramphenicol	Sigma-Aldrich	Cat#:C1919-25G	34 mg/ml in ethanol (stored at -20 °C)

drug	Ampicillin	Sigma-Aldrich	Cat#: A9518-5G	50 mg/ml in ddH ₂ O (stored at -80 °C)
other	pooled human female urine	Golden West Diagnostics	Cat#: OH2010-pH	
other	Phosphate Buffered Saline	Thermofisher	Cat#: 10010056	
other	Gibco™ HEPES	Thermofisher	Cat#: F2006	
other	Invitrogen™ DAPI	Thermofisher	Cat#: D1306	5 mg/ml in DMSO
other	LB (Luria broth base, Miller's modified)	Sigma-Aldrich	Cat#: L1900-1KG	
other	Organ-chips (Standard Research Kit - 24 per Pack)	Emulate	RE1000001024	
other	CellMask™ Orange Plasma membrane Stain	Thermofisher	Cat#: C10045	1µM in cell media
other	HCS CellMask™ Deep Red Stain	Thermofisher	Cat#: H32721	2µM in PBS
other	CellTracker™ Deep Red Dye	Thermofisher	Cat#: C34565	1µM in cell media
other	Elveflow® OB1 Pressure Controller OB1 Base MkIII+	Elveflow	Cat#: OB1MKIII+-MIX-	connected to 6bar compressed air channel
other	Elveflow® OB1 Pressure Controller OB1 MkIII Channel-900/1000	Elveflow	Cat#: OB1-Dual-	connected to Elveflow® OB1 Pressure Controller OB1 Base MkIII+
other	Diaphragm moist gas vacuum pump	KNF Neuberger	Cat#:LABOPORT® UN 820.3 FT.40P	connected to Elveflow® OB1 Pressure Controller OB1 MkIII Channel-900/1000
antibody	Anti-EpCAM (rabbit polyclonal)	abcam	Cat#: ab71916	IF (1:100) in 1% BSA
antibody	Anti-PECAM1 or Anti-CD31 (mouse monoclonal)	abcam	Cat#: ab24590	IF (1:100) in 1% BSA
antibody	Anti-CK7 (rabbit monoclonal)	abcam	Cat#: ab209599	IF (1:100) in 1% BSA
antibody	Anti-CK8 (rabbit monoclonal)	abcam	Cat#: ab192468	IF (1:100) in 1% BSA
other	Alexa Fluor™ 555 Phalloidin	Thermofisher	Cat#: A34055	1µM in PBS
antibody	Anti-VE-Cadherin (rabbit polyclonal)	abcam	Cat#: ab33168	IF (1:100) in 1% BSA
antibody	Anti-Uroplakin3a (mouse monoclonal)	Santa Cruz	Cat#: sc-166808	IF (1:100) in 1% BSA

antibody	Anti-CK1 (mouse monoclonal)	Thermofisher	Cat#: MA1-06312	IF (1:100) in 1% BSA
antibody	Anti-E-Cadherin (mouse monoclonal)	Thermofisher	Cat#: MA5-14408	IF (1:100) in 1% BSA
antibody	Anti-ZO-1 (rabbit polyclonal)	abcam	Cat#: ab216880	IF (1:100) in 1% BSA
antibody	Anti-myeloperoxidase (rabbit polyclonal)	abcam	Cat#: ab9535	IF (1:100) in 1% BSA
antibody	Anti-neutrophil elastase (rabbit polyclonal)	abcam	Cat#: ab68672	IF (1:100) in 1% BSA
antibody	Anti-CD15 (mouse monoclonal)	abcam	Cat#: ab665	IF (1:100) in 1% BSA
antibody	Donkey anti-Mouse IgG (H+L) Highly Cross-Adsorbed Secondary Antibody, Alexa Fluor 647	Thermofisher	Cat#: A-31571	IF (2 µg/ml)
antibody	Donkey anti-Rabbit IgG (H+L) Highly Cross-Adsorbed Secondary Antibody, Alexa Fluor 647	Thermofisher	Cat#: A-31573	IF (2 µg/ml)
antibody	Goat anti-Mouse IgG (H+L) Highly Cross-Adsorbed Secondary Antibody, Alexa Fluor 488	Thermofisher	Cat#: A-11029	IF (2 µg/ml)
antibody	Donkey anti-Rabbit IgG (H+L) Highly Cross-Adsorbed Secondary Antibody, Alexa Fluor 568	Thermofisher	Cat#: A10042	IF (2 µg/ml)
antibody	Donkey anti-Mouse IgG (H+L) Highly Cross-Adsorbed Secondary Antibody, Alexa Fluor 568	Thermofisher	Cat#: A10037	IF (2 µg/ml)
peptide, recombinant protein	Fibronectin from human plasma	Sigma-Aldrich	Cat#: F1056	500 µg/ml in ddH ₂ O
peptide, recombinant protein	Native Collagen, Bovine dermis	AteloCell	Cat#: IAC-50	5 mg/ml
peptide, recombinant protein	Human IL-1α, research grade	Miltenyi Biotec	Cat#:130-093-894	1 µg/ml
peptide, recombinant protein	Human IL-1β, research grade	Miltenyi Biotec	Cat#:130-093-895	1 µg/ml
peptide, recombinant protein	Human IL-6, research grade	Miltenyi Biotec	Cat#:130-093-929	1 µg/ml

peptide, recombinant protein	Human IL-8, research grade	Miltenyi Biotec	Cat#:130-122-354	1 µg/ml
commercial assay or kit	MACSxpress® Whole Blood Neutrophil Isolation Kit, human	Miltenyi Biotec	Cat#:130-104-434	
software, algorithm	Imaris 9.5.1	Bitplane		
other	Gas chamber for stages with k-frame insert (160x110mm) - magnetic model with sliding lid.	okolab	Cat#: H201-K-FRAME	
other	Custom holder for 24mm x 60mm coverslip	okolab	Cat#:1x24by60-M	
other	µ-Slide 8 Well	ibidi	Cat#:80826	
other	Masterflex PharMed tubing, 0.89mm ID, 100 ft	Cole-Palmer	Cat#:GZ-95709-26	
other	Masterflex® Transfer Tubing, Tygon® 0.76mm ID	Cole-Palmer	Cat#:GZ-06419-03	
other	1.30 x 0.75 x 10 mm metallic tubes	Unimed	Cat#:9084 / 200.010-A	
other	1.00/0.75 x 20mm metallic tubes	Unimed	Cat#:200.010-A	
other	Aladdin programmable pump	WPI	Cat#: PUMP-NE-1000	

1001

1002 **Cell Lines**

1003 5637 human bladder epithelial carcinoma cell line (procured from ATCC, HTB-9™). Cell line

1004 tested negative for mycoplasma contamination.

1005

1006 **Cell culture of human bladder epithelial and bladder endothelial cells**

1007 The 5637 human bladder epithelial carcinoma cell line (ATCC, HTB-9™) was cultured in RPMI

1008 1640 medium supplemented with 10% Fetal Bovine Serum (FBS) as recommended by the

1009 supplier. Human Primary Bladder Epithelial cells (Cell Biologics, H-6215) were cultured in

1010 complete epithelial cell medium supplemented with growth factors as recommended by the

1011 supplier. Human Bladder Microvascular Endothelial cells (HMVEC-Bd) (Lonza, CC-7016) were

1012 cultured in Lonza EGM-2 MV BulletKit medium. Both the epithelial and endothelial cells were

cultured in their respective medium supplemented with 1X Antibiotic-Antimycotic solution. Epithelial cells were passaged by detachment with 0.05% Trypsin at 37°C for 3-5 minutes followed by neutralization of trypsin with RPMI 1640 medium/10% FBS. Bladder endothelial cells were passaged and split as recommended by the supplier. The cells used in all the experiments were at ten passages or fewer. The cell lines were tested routinely for mycoplasma contamination during passaging.

UPEC culture for infection of bladder epithelial cells in the bladder-chip

Uropathogenic *Escherichia coli* (UPEC) strain CFT073 was originally isolated from a pyelonephritis patient (Mobley et al., 1990) and provided by Prof. H.L.T. Mobley, University of Michigan, USA. A derivative strain expressing yellow fluorescent protein (YFP) was generated by electroporation of CFT073 with the episomal plasmid pZA32-YFP (Lutz and Bujard, 1997), as described earlier (Dhar et al., 2015). To induce expression of type 1 pili, UPEC was grown in LB media containing 25 µg/ml chloramphenicol under non-shaking conditions at 37 °C for 2 days prior to the experiment, to achieve a stationary phase culture ($OD_{600}=1.5$ and corresponding to a concentration of 1.5×10^9 bacteria/ml). The bacteria were diluted 10-fold to a final concentration of 1.5×10^8 cells/ml) and resuspended in a solution of pooled human female urine (Golden West Diagnostics Catalogue OH2010-pH) diluted 10-fold in Phosphate Buffered Saline.

Recapitulation of human bladder physiology in human bladder-on-a-chip device

Bladder-chip devices made of polydimethylsiloxane (PDMS) were purchased from Emulate (Boston, USA). The dimensions of the microfluidic device were as follows: width of the channels- 1000 µm, height of the upper channel- 1000 µm, lower channel – 250 µm). For

extracellular matrix (ECM) coating, a coating solution consisting of the ER-1 compound (Emulate) dissolved in ER-2 solution at 0.5 mg/ml (Emulate) was introduced in both apical and vascular channels and the chips were subsequently activated by exposing the bladder-chip for 20 minutes under UV light. The channels were then rinsed with fresh coating solution and the protocol was repeated once again. The channels of the bladder-chip were then washed thoroughly with PBS before incubation with an ECM solution of 150 µg/ml bovine collagen type I and 30 µg/ml fibronectin from human plasma in PBS buffered with 15 mM HEPES solution for 1-2 hours at 37°C as described previously (Thacker et al., 2020). If not used directly, coated chips were stored at 4°C and pre-activated before use by incubation for 30 minutes with the same ECM solution at 37°C. Three days before the day of the experiment, HMVEC-Bd cells were seeded into lower channel of the inverted bladder-chip device at 0.5 million cells/ml. Two days before the experiment, 5637 cells were seeded into upper channel at 5 million cells/ml. Prior to the infection experiment, bladder endothelial and bladder epithelial cells were cultured in their respective medium supplemented with the 1X Antibiotic-Antimycotic solution. The antibiotics were removed prior to the experiment.

Characterization and immunostaining of human bladder epithelial and human bladder epithelial cells in ibidi wells and human bladder-chip

Human bladder epithelial and bladder endothelial cells were cultured inside ibidi µ-Slide 8 wells for one day. The cells were subsequently fixed with 4% paraformaldehyde (PFA) for 30 minutes at room temperature. Fixed cells were then washed three times with 200 µl of PBS to remove residues of PFA, permeabilized with 0.15 % Triton X-100 for 15 minutes; washed three times with 200 µl of PBS to remove residues of detergent and then incubated in a blocking solution of

1% BSA in PBS for 1 hour. The cells were then incubated with primary antibodies (anti-EpCAM, anti-PECAM-1, anti-CK7, anti-CK8, anti-VE-Cadherin, anti-Uroplakin3a, anti-CK1, anti-E-Cadherin, anti-ZO-1, anti-myeloperoxidase, anti-neutrophil elastase, anti-CD15) at a dilution of 1:100 in an antibody incubation buffer comprising 1% BSA and 0.01% Triton-100 in PBS. The ibidi 8-wells were subsequently washed three times with PBS for 10 minutes each. Incubation with secondary antibody (Donkey anti-Mouse Alexa Fluor 647, Donkey anti-Mouse Alexa Fluor 568, Goat anti-Mouse Alexa Fluor 488, Donkey anti-Rabbit Alexa Fluor 647, Donkey anti-Rabbit Alexa Fluor 568, Donkey anti-Rabbit Alexa Fluor 488) at a concentration of 2 µg/ml in antibody incubation buffer was subsequently performed for 1 hour at room temperature. Excess antibody was removed by washing three times with PBS for 10 minutes each. Cell nuclei were stained with DAPI (5 µg/ml) solution in PBS for 30 minutes. Ibidi 8-wells were washed three times to remove unbound DAPI. Cells were covered with appropriate volume of PBS until imaging. Cells were imaged with 63X oil objective on Leica SP8 confocal microscope. Images were deconvolved using SVI Huygens (Quality, 0.05; Iterations, 40).

For characterization of the cell types on-chip, bladder-chips with co-culture of bladder epithelial and bladder endothelial cells were kept under pooled diluted urine and EBM2 medium using P200 pipette tips for 2 days prior to PFA fixation. The cells in the bladder-chip were then immunostained following the protocol described above. Images were acquired with Leica HC FLUOTAR 25X (NA 0.95) multi-immersion objective on Leica SP8 confocal microscope.

Characterization of strain-pressure curve in the bladder-chip model

Elveflow OB1 MK3 – Microfluidic flow control system was used to control the negative pressure applied to the human bladder-chip. The control system was connected to the compressed air line (6 bar) for the positive pressure and diaphragm vacuum pump for the negative pressure. A negative pressure (0 to -900 mbar) with a step function of -100mbar was subsequently applied to the vacuum channels in the bladder-chip using a Pressure Controller (Elveflow OB1 pressure controller). For these experiments, both bladder epithelial and endothelial cells were seeded on the respective sides in the devices. This experiment was performed with the chip maintained on the stage of the microscope and a brightfield image was acquired at each step increase of -100mbar, on Leica SP8 confocal microscope. The PDMS inter-pore-to-pore distance was measured for 14 pore-to-pore combinations at each input of negative pressure. Linear fitting was performed using GraphPad Prism (version 9).

Mimicking bladder filling and voiding cycle in human bladder-chip

The stretching of the human bladder-chip was done using the Elveflow OB1 MK3 – Microfluidic flow control system connected to the compressed air line (6 bar) for the positive pressure and diaphragm vacuum pump for the negative pressure. Human bladder-chip in the relaxed (*voided bladder*, 0% strain) state was slowly perturbed with a linear ramp function to reach a stretched (*filled bladder*, 10% strain) state over a period of 2 hours. Linear strain of 10% strain was achieved by application of ca. 520-530 mbar negative pressure in the vacuum channels. This period corresponded to the *filling bladder* state in [Figure 1D](#). Bladder-chip was kept under stretched (*filled bladder*, 10% strain) state over the subsequent 2 hours. Micturition or urination was recapitulated by rapidly reducing the applied strain on the bladder-chip from the stretched (*filled bladder*, 10% strain) state to relaxed (*voided bladder*, 0% strain) state over a period of 2

minutes. Subsequently, the bladder-chip was maintained with no negative pressure applied in the vacuum channel under relaxed (*voided bladder*, 0% strain) state from (4:02 hours to 6 hours). This 6-hour bladder filling and voiding cycle was repeated continuously for the rest of the experiment.

Experimental setup and imaging parameters for time lapse imaging for UPEC infection in the human bladder-chip devices

The medium perfusion inside the bladder-chip device was achieved with the Aladdin syringe pumps. The syringes with respective media were connected to the bladder-chip via gas impermeable PharMed® tubing (inner diameter =0.89 mm, Cole palmer GZ-95809-26) along with longer transparent Tygon tubings (internal diameter of 0.76mm, Masterflex transfer tubing, Cole palmer). The PharMed® tubing was connected to the inlet and outlet of the bladder-chip with 1.30 x 0.75 x 10 mm metallic tubes (Unimed) and transparent tubing with 1.00/0.75 x 20mm metallic tubes (Unimed). The bladder-chip connected to external sources of flow was then mounted onto a 24 x 60 mm No. 1 glass coverslip for microscopy imaging. When required for stretching experiments, tubing was also connected to the stretching channels on either side of the main channel. The connected device was subsequently assembled inside a temperature-controlled microscope environmental chamber at 37°C supplemented with 5% CO₂ (OKO labs). Time-lapse imaging was conducted using a Leica HC FLUOTAR 25X (NA 0.95) multi-immersion objective within custom made environmental chamber set at 37°C for infusion with syringe pumps. Water was pumped to the ring around the water objective at 9 Hz with pumping duration of 9 seconds and pumping interval 30 minutes, controlled by SRS software (HRZ=9, VPP=95). The autofocus mode (best focus, steps =9, range = 30 µm) was used to maintain the optical focus on the apical side of the PDMS membrane. The experiments were monitored

frequently to ensure that the optical focus was maintained, and the experiment was halted and restarted if the focus was lost.

To enable rapid 3-D imaging across multiple spatial locations on-chip, we utilized the capability of the white light laser on the Leica SP8 confocal microscope to image at multiple wavelengths simultaneously. The excitation wavelengths were grouped into two sequences to minimize the spectral overlap. In the first sequence, laser emission at 555 nm was used to excite the CellMask Orange stain in the bladder epithelial cells. In the second laser excitation sequence, laser emission at 500 nm and 630 nm were used to excite the YFP within the bacteria and the cytoplasmic CellTrackerTM Deep Red in the human neutrophils. Images were acquired with a scan speed of 400-700 Hz and a zoom factor of 2.25 (206.67 μm x 206.67 μm) resulting in an XY resolution of 450 nm depending on the number of pixels acquired per field of view. Z-stacks were acquired with 1 μm step sizes. Time lapse images were acquired with interval duration of ca. 15-17 minutes, in a subset of experiments this was further reduced to 7.5 minutes by imaging with the second sequence only at a z-step size of 2 μm .

Time lapse imaging for UPEC infections in the human bladder-chip devices

Pre-infection stage

The time-course of the entire experimental protocol is shown in a schematic in [Figure 1E](#). The bladder-chip device was perfused with diluted urine in the apical channel and EBM Endothelium phenol-red free medium supplemented with EGM-2 endothelial SingleQuots kit in the vascular channel. Prior to the commencement of infection, the chip was maintained at homeostasis and the epithelial cells were imaged for a period of two hours.

1150 Infection stage

1151 Stationary phase UPEC in diluted pooled urine at a concentration of 150 million cells/ml were
1152 flowed through the apical channel of the device at 1200 $\mu\text{l}/\text{hour}$ for 1.5 hours. During this period,
1153 EBM2 media was flowed through the endothelial channel at 600 $\mu\text{l}/\text{hour}$.

1154

1155 Bacterial washout and neutrophil introduction stage

1156 Next, the syringe connected to the apical channel was replaced with a fresh syringe containing
1157 pooled diluted urine, this solution was then flowed in the apical channel over the epithelial layer
1158 of the chip at a flow rate of 600 $\mu\text{l}/\text{hour}$ over the next 3 hours. This allowed for the continuous
1159 removal of extracellular planktonic bacteria in the apical channel. At the same time, human
1160 neutrophils were introduced into the endothelial channel of the bladder-chip via flow. A solution
1161 of human neutrophils at a density of 2 million cells/ml isolated via negative selection was flowed
1162 through the vascular channel for 3 hours in EBM2 medium with at higher shear stress of $\eta=1.0$
1163 dyne/cm^2 to enhance neutrophil attachment to endothelial cells.

1164

1165 Neutrophil diapedesis stage

1166 Diapedesis of human neutrophils to epithelial side and subsequent interactions of neutrophils
1167 with UPEC was observed for the subsequent 3 hours since introduction of neutrophils into the
1168 vasculature side of the chip. During this period, the flow rate in the apical and vascular channels
1169 were maintained at 600 $\mu\text{l}/\text{hour}$ and 3000 $\mu\text{l}/\text{hour}$, respectively. During this period, in a subset of
1170 experiments, only the channels that were part of the second laser scanning sequence were
1171 imaged. Images of the CellTracker Orange dye for epithelial cell identification were not acquired
1172 (first laser scanning sequence). This enabled a number of fields of view to be captured with an

enhanced temporal resolution and a frame rate of up to 7.5 minutes. For experiments studying the formation of NETs, the experiment was halted at this stage and the infected chips were fixed, permeabilized, blocked, and immunostained with anti-myeloperoxidase (abcam) or anti-neutrophil elastase (abcam) antibodies using the procedure described earlier. For all other experiments, live imaging continued to the subsequent antibiotic treatment phase.

Antibiotic treatment and growth cycles

Thereafter, syringes connected to both apical and vascular channels were changed and ampicillin at 250 µg/ml (used at ~40-fold over the minimum inhibitory concentration (MIC) of ampicillin against UPEC grown in EBM2 medium) was introduced both in the diluted urine and the EBM2 media perfused into the apical and vascular channels, respectively, for 3 hours at a flow rate of 600 µl/hour. This was the first ampicillin treatment cycle; whose purpose was to eliminate extracellular bacteria in the apical channel and allow intracellular bacterial colonies (IBCs) to be identified. The urine and EBM2 media were subsequently switched in the respective channels with antibiotic-free medium for next 8 hours to allow for IBC growth within epithelial cells. During this period, the flow within the apical channel was maintained, to remove bacteria that grew extracellularly either because they survived the antibiotic treatment or that were released from infected epithelial cells. The ampicillin and growth cycle were then repeated, to allow the assessment of the response of bacteria within IBCs to antibiotic treatment as well as characterize the subsequent regrowth.

Image analysis of confocal live-cell images

Image analysis was performed with Bitplane Imaris 9.5.1. The time-lapse imaging stack included five channels: uroepithelial cells (epithelial channel), transmitted light (bright field channel), UPEC (bacterial channel), neutrophils (neutrophil channel), and transmitted light (bright field channel). Neutrophils were identified via the spot detection algorithm in Imaris used on the images from the neutrophil channel with the following parameters (Size, 8 μm ; Quality, 4 to 8). Swarms of neutrophils generate dense aggregates that are ill-suited to quantification with the spot detection algorithm. To quantify the size of the swarms, we therefore segmented images in the neutrophil channel to generate surfaces via the automatic segmentation tool in Imaris with the following parameters (Threshold, 10; Smooth Surfaces Detail, 0.5 or 1.0 μm). Unfortunately, the time resolution was insufficient to track individual neutrophils over time particularly since neutrophils formed small clumps and rapidly changed their cell shapes. For UPEC volume inside IBCs, necessary 3D volume was cropped in Imaris to ease image analysis. Total bacterial volume inside IBC was detected by creating the surface (Threshold, 15; Smooth Surfaces Detail, 0.5 or 1 μm) on UPEC channel. In cases of measuring extracellular UPEC growth, surface was generated (Threshold, 15; Smooth Surfaces Detail, 0.5 or 1 μm) on UPEC channel to calculate total extracellular volume in the field of view.

Isolation and labelling of human neutrophils from fresh human blood

Fresh human blood was procured from voluntary donations by anonymised healthy donors via the Transfusion Interregionale CRS network based in Bern, Switzerland. Donors were made aware that their donation could be used for biomedical research. No personal information about the donors was available to the end users, therefore the consent to publish could not be obtained.

1218 Approval for this use of blood was provided by the Transfusion Interregionale CRS network
1219 (project number P_257). Human neutrophils were isolated via negative depletion method from
1220 human blood with MACSxpress® Whole Blood Neutrophil Isolation Kit (Miltenyi Biotec),
1221 following the manufacturer's instructions. Isolation was performed without the use of a density-
1222 based centrifugation method. Isolated human neutrophils were then incubated with a 1µM
1223 solution CellTracker™ Deep Red in a serum free RPMI phenol red free medium for 30 minutes
1224 in a cell culture incubator maintained at 37 C and 5% CO₂. Labelled human neutrophils were
1225 then washed with 10 ml of 20% FBS in RPMI phenol red free medium followed by
1226 centrifugation twice to remove the unbound dye. The human neutrophils were suspended in
1227 Lonza EBM2 medium at a cell density of 2 million cells/ml. In some instances, labelled human
1228 neutrophils were passed through a filter with 40 µm pores to remove neutrophil clusters that may
1229 have formed during the isolation process.

1230

1231 **Scanning electron microscopy of human bladder-chip**

1232 UPEC within infected human bladder-chips were allowed to proliferate for 6 hours (ca. 13.5
1233 hours from start of UPEC infection) until the end of the first IBC growth cycle. After 6 hours,
1234 human bladder-chip was fixed at room temperature for 1 hour with a mix of 1% glutaraldehyde
1235 and 2% paraformaldehyde in 0.1 M phosphate buffer (pH 7.4). The fixed bladder-chip was kept
1236 in the fixative overnight (at 4°C). Post overnight fixation, human bladder-chip was cut open from
1237 the apical channel side. A scalpel was used to cut approximately in the middle of the apical
1238 channel side (height=1mm) to expose the bladder epithelial cells. The fixed chip was further
1239 fixed for 30 minutes in 1% osmium tetroxide in 0.1 M cacodylate buffer followed by washing
1240 with the distilled water. Next, the bladder-chip was dehydrated in a graded alcohol series and

dried by passing them through the supercritical point of carbon dioxide (CPD300, Leica Microsystems). Finally, the bladder-chip was attached to an adhesive conductive surface followed by coating with a 3 – 4 nm thick layer of gold palladium metal (Quorum Q Plus, Quorum Technologies). Images of the cells were captured using a field emission scanning electron microscope (Merlin, Zeiss NTS).

Uninfected human bladder-chip controls were fixed at the same time point (ca. 13.5 hours from start of the experiment). For the case of NETs formed on epithelial layer, an uninfected human bladder-chip was fixed 2 hours after the introduction of neutrophils into the vascular channel of the chip.

Preparation for transmission electron microscopy (TEM)

UPEC within infected human bladder-chips were allowed to proliferate for 6 hours (ca. 13.5 hours from start of UPEC infection) during the first IBC growth cycle. After 6 hours, human bladder-chip was fixed at room temperature for 1 hour with a mix of 1% glutaraldehyde and 2% paraformaldehyde in 0.1 M phosphate buffer (pH 7.4). The fixed bladder-chip was kept in the fixative overnight (at 4°C). Post overnight fixation, human bladder-chip was cut open from the apical channel side. A scalpel was used to cut approximately in the middle of the apical channel side (height-1mm) to expose the bladder epithelial cells. The bladder-chip was then washed in cacodylate buffer (0.1M, pH 7.4), postfixed for 40 minutes in 1.0 % osmium tetroxide with 1.5% potassium ferrocyanide, and then fixed again with 1.0% osmium tetroxide alone. The bladder-chip was finally stained for 30 minutes in 1% uranyl acetate in water before being dehydrated through increasing concentrations of alcohol and then embedded in Durcupan ACM (Fluka, Switzerland) resin. The bladder-chip was then placed in Petri dishes so that approximately 1 mm

of resin remained above the cells, and the dish than left in an oven at 65°C for 24 hours. Regions on interest, and corresponding to structures imaged with light microscopy were trimmed from the rest of the device, once the resin had hardened, and thin, 50 nm-thick sections were cut with a diamond knife, and collected onto single-slot copper grids with a pioloform support film. These were contrasted with lead citrate and uranyl acetate, and images taken with a transmission electron microscope at 80 kV (Tecnai Spirit, FEI Company with Eagle CCD camera).

Data availability statement

Source data for Figures 1 – 4 and the accompanying Figure Supplements have been uploaded to the EPFL community pages at Zenodo and are available at the following doi: 10.5281/zenodo.5028262.

1276

1277 **Bibliography**

1278

1279 Abraham, S.N., and Miao, Y. (2015). The nature of immune responses to urinary tract infections.
1280 *Nat Rev Immunol* 15, 655–663.

1281 Agace, W.W., Hedges, S.R., Ceska, M., and Svanborg, C. (1993). Interleukin-8 and the
1282 neutrophil response to mucosal gram-negative infection. *J Clin Invest* 92, 780–785.

1283 Agace, W.W., Patarroyo, M., Svensson, M., Carlemalm, E., and Svanborg, C. (1995).
1284 *Escherichia coli* induces transuroepithelial neutrophil migration by an intercellular adhesion
1285 molecule-1-dependent mechanism. *Infect Immun* 63, 4054–4062.

1286 Alon, R., Hammer, D.A., and Springer, T.A. (1995). Lifetime of the P-selectin-carbohydrate
1287 bond and its response to tensile force in hydrodynamic flow. *Nature* 374, 539–542.

1288 Andersen, T.E., Khandige, S., Madelung, M., Brewer, J., Kolmos, H.J., and Møller-Jensen, J.
1289 (2012). *Escherichia coli* uropathogenesis in vitro: invasion, cellular escape, and secondary
1290 infection analyzed in a human bladder cell infection model. *Infect Immun* 80, 1858–1867.

1291 Anderson, G.G., Palermo, J.J., Schilling, J.D., Roth, R., Heuser, J., and Hultgren, S.J. (2003).
1292 Intracellular Bacterial Biofilm-Like Pods in Urinary Tract Infections. *Science* 301, 105–107.

1293 Apodaca, G. (2004). The Uroepithelium: Not Just a Passive Barrier. *Traffic* 5, 117–128.

1294 Benam, K.H., Villenave, R., Lucchesi, C., Varone, A., Hubeau, C., Lee, H.-H., Alves, S.E.,
1295 Salmon, M., Ferrante, T.C., Weaver, J.C., et al. (2016). Small airway-on-a-chip enables analysis
1296 of human lung inflammation and drug responses in vitro. *Nat Methods* 13, 151–157.

1297 Bergan, T. (1990). Degree of absorption, pharmacokinetics of fosfomycin trometamol and
1298 duration of urinary antibacterial activity. *Infection* 18, S65–S69.

1299 Blango, M.G., and Mulvey, M.A. (2010). Persistence of Uropathogenic *Escherichia coli* in the
1300 Face of Multiple Antibiotics ▽. *Antimicrob Agents Ch* 54, 1855–1863.

1301 Brinkmann, V., Reichard, U., Goosmann, C., Fauler, B., Uhlemann, Y., Weiss, D.S., Weinrauch,
1302 Y., and Zychlinsky, A. (2004). Neutrophil Extracellular Traps Kill Bacteria. *Science* 303, 1532–
1303 1535.

1304 Bryskier, A. (2020). Antimicrobial Agents: Antibacterials and Antifungals. pp. 113–162.

1305 Cakir, B., Xiang, Y., Tanaka, Y., Kural, M.H., Parent, M., Kang, Y.-J., Chapeton, K., Patterson,
1306 B., Yuan, Y., He, C.-S., et al. (2019). Engineering of human brain organoids with a functional
1307 vascular-like system. *Nat Methods* 16, 1169–1175.

1308 Carattino, M.D., Prakasam, H.S., Ruiz, W.G., Clayton, D.R., McGuire, M., Gallo, L.I., and
 1309 Apodaca, G. (2013). Bladder filling and voiding affect umbrella cell tight junction organization
 1310 and function. *Am J Physiol-Renal* 305, F1158–F1168.

1311 Clevers, H. (2016). Modeling Development and Disease with Organoids. *Cell* 165, 1586–1597.

1312 Dhar, N., Dubée, V., Ballell, L., Cuinet, G., Hugonnet, J.-E., Signorino-Gelo, F., Barros, D.,
 1313 Arthur, M., and McKinney, J.D. (2015). Rapid Cytolysis of Mycobacterium tuberculosis by
 1314 Faropenem, an Orally Bioavailable β -Lactam Antibiotic. *Antimicrob Agents Ch* 59, 1308–1319.

1315 Duncan, M.J., Li, G., Shin, J.-S., Carson, J.L., and Abraham, S.N. (2004). Bacterial Penetration
 1316 of Bladder Epithelium through Lipid Rafts. *J Biol Chem* 279, 18944–18951.

1317 Duraiswamy, S., Chee, J.L.Y., Chen, S., Yang, E., Lees, K., and Chen, S.L. (2018). Purification
 1318 of Intracellular Bacterial Communities during Experimental Urinary Tract Infection Reveals an
 1319 Abundant and Viable Bacterial Reservoir. *Infect Immun* 86, e00740-17.

1320 Ermert, D., Urban, C.F., Laube, B., Goosmann, C., Zychlinsky, A., and Brinkmann, V. (2009).
 1321 Mouse Neutrophil Extracellular Traps in Microbial Infections. *J Innate Immun* 1, 181–193.

1322 Fedrigo, N.H., Mazucheli, J., Albiero, J., Shinohara, D.R., Lodi, F.G., Machado, A.C. dos S., Sy,
 1323 S.K.B., and Tognim, M.C.B. (2017). Pharmacodynamic Evaluation of Fosfomycin against
 1324 Escherichia coli and Klebsiella spp. from Urinary Tract Infections and the Influence of pH on
 1325 Fosfomycin Activities. *Antimicrob Agents Ch* 61, e02498-16.

1326 Foxman, B. (2010). The epidemiology of urinary tract infection. *Nat Rev Urol* 7, 653–660.

1327 Gloeckner, D.C., SACKS, M.S., FRASER, M.O., SOMOGYI, G.T., GROAT, W.C. de, and
 1328 CHANCELLOR, M.B. (2002). Passive Biaxial Mechanical Properties of the Rat Bladder Wall
 1329 After Spinal Cord Injury. *J Urology* 167, 2247–2252.

1330 Grassart, A., Malardé, V., Gobba, S., Sartori-Rupp, A., Kerns, J., Karalis, K., Marteyn, B.,
 1331 Sansonetti, P., and Sauvonnnet, N. (2019). Bioengineered Human Organ-on-Chip Reveals
 1332 Intestinal Microenvironment and Mechanical Forces Impacting Shigella Infection. *Cell Host*
 1333 *Microbe* 26, 435-444.e4.

1334 Hannan, T.J., Totsika, M., Mansfield, K.J., Moore, K.H., Schembri, M.A., and Hultgren, S.J.
 1335 (2012). Host–pathogen checkpoints and population bottlenecks in persistent and intracellular
 1336 uropathogenic Escherichia coli bladder infection. *Fems Microbiol Rev* 36, 616–648.

1337 Haraoka, M., Hang, L., Frendéus, B., Godaly, G., Burdick, M., Strieter, R., and Svanborg, C.
 1338 (1999). Neutrophil Recruitment and Resistance to Urinary Tract Infection. *J Infect Dis* 180,
 1339 1220–1229.

1340 Hedges, S., Svensson, M., and Svanborg, C. (1992). Interleukin-6 response of epithelial cell lines
 1341 to bacterial stimulation in vitro. *Infect Immun* 60, 1295–1301.

1342 Horsley, H., Dharmasena, D., Malone-Lee, J., and Rohn, J.L. (2018). A urine-dependent human
 1343 urothelial organoid offers a potential alternative to rodent models of infection. *Sci Rep-Uk* 8,
 1344 1238.

1345 Hsieh, M.M., Everhart, J.E., Byrd-Holt, D.D., Tisdale, J.F., and Rodgers, G.P. (2007).
 1346 Prevalence of Neutropenia in the U.S. Population: Age, Sex, Smoking Status, and Ethnic
 1347 Differences. *Ann Intern Med* 146, 486.

1348 Huh, D., Matthews, B.D., Mammoto, A., Montoya-Zavala, M., Hsin, H.Y., and Ingber, D.E.
 1349 (2010a). Reconstituting Organ-Level Lung Functions on a Chip. *Science* 328, 1662–1668.

1350 Huh, D., Matthews, B.D., Mammoto, A., Montoya-Zavala, M., Hsin, H.Y., and Ingber, D.E.
 1351 (2010b). Reconstituting Organ-Level Lung Functions on a Chip. *Science* 328, 1662–1668.

1352 Hung, C.-S., Dodson, K.W., and Hultgren, S.J. (2009). A murine model of urinary tract
 1353 infection. *Nat Protoc* 4, 1230–1243.

1354 Hunstad, D.A., and Justice, S.S. (2010). Intracellular Lifestyles and Immune Evasion Strategies
 1355 of Uropathogenic *Escherichia coli*. *Annu Rev Microbiol* 64, 203–221.

1356 Iosifidis, G., and Duggin, I.G. (2020). Distinct Morphological Fates of Uropathogenic
 1357 *Escherichia coli* Intracellular Bacterial Communities: Dependency on Urine Composition and
 1358 pH. *Infect Immun* 88.

1359 Jalili-Firoozinezhad, S., Gazzaniga, F.S., Calamari, E.L., Camacho, D.M., Fadel, C.W., Bein, A.,
 1360 Swenor, B., Nestor, B., Cronce, M.J., Tovaglieri, A., et al. (2019). A complex human gut
 1361 microbiome cultured in an anaerobic intestine-on-a-chip. *Nat Biomed Eng* 3, 520–531.

1362 Jang, K.-J., Mehr, A.P., Hamilton, G.A., McPartlin, L.A., Chung, S., Suh, K.-Y., and Ingber,
 1363 D.E. (2013). Human kidney proximal tubule-on-a-chip for drug transport and nephrotoxicity
 1364 assessment. *Integr Biol* 5, 1119–1129.

1365 Jang, K.-J., Otieno, M.A., Ronxhi, J., Lim, H.-K., Ewart, L., Kodella, K.R., Petropolis, D.B.,
 1366 Kulkarni, G., Rubins, J.E., Conegliano, D., et al. (2019). Reproducing human and cross-species
 1367 drug toxicities using a Liver-Chip. *Sci Transl Med* 11, eaax5516.

1368 Justice, S.S., Hung, C., Theriot, J.A., Fletcher, D.A., Anderson, G.G., Footer, M.J., and Hultgren,
 1369 S.J. (2004). Differentiation and developmental pathways of uropathogenic *Escherichia coli* in
 1370 urinary tract pathogenesis. *Proc National Acad Sci* 101, 1333–1338.

1371 Kang, Y.B. (Abraham), Rawat, S., Duchemin, N., Bouchard, M., and Noh, M. (2017). Human
 1372 Liver Sinusoid on a Chip for Hepatitis B Virus Replication Study. *Micromachines-Basel* 8, 27.

1373 Kienle, K., and Lämmermann, T. (2016). Neutrophil swarming: an essential process of the
 1374 neutrophil tissue response. *Immunol Rev* 273, 76–93.

1375 Kim, H.J., and Ingber, D.E. (2013). Gut-on-a-Chip microenvironment induces human intestinal
1376 cells to undergo villus differentiation. *Integr Biol* 5, 1130–1140.

1377 Kim, H.J., Li, H., Collins, J.J., and Ingber, D.E. (2016). Contributions of microbiome and
1378 mechanical deformation to intestinal bacterial overgrowth and inflammation in a human gut-on-
1379 a-chip. *Proc National Acad Sci* 113, E7–E15.

1380 Klein, R.D., and Hultgren, S.J. (2020). Urinary tract infections: microbial pathogenesis, host-
1381 pathogen interactions and new treatment strategies. *Nat Rev Microbiol* 18, 211–226.

1382 Kong, X.-T., Deng, F.-M., Hu, P., Liang, F.-X., Zhou, G., Auerbach, A.B., Genieser, N., Nelson,
1383 P.K., Robbins, E.S., Shapiro, E., et al. (2004). Roles of uroplakins in plaque formation, umbrella
1384 cell enlargement, and urinary tract diseases. *J Cell Biology* 167, 1195–1204.

1385 Korkmaz, I., and Rogg, B. (2007). A simple fluid-mechanical model for the prediction of the
1386 stress–strain relation of the male urinary bladder. *J Biomech* 40, 663–668.

1387 Kreisel, D., Nava, R.G., Li, W., Zinselmeyer, B.H., Wang, B., Lai, J., Pless, R., Gelman, A.E.,
1388 Krupnick, A.S., and Miller, M.J. (2010). In vivo two-photon imaging reveals monocyte-
1389 dependent neutrophil extravasation during pulmonary inflammation. *Proc National Acad Sci*
1390 107, 18073–18078.

1391 Lämmermann, T., Afonso, P.V., Angermann, B.R., Wang, J.M., Kastenmüller, W., Parent, C.A.,
1392 and Germain, R.N. (2013). Neutrophil swarms require LTB4 and integrins at sites of cell death
1393 in vivo. *Nature* 498, 371–375.

1394 Ley, K., Laudanna, C., Cybulsky, M.I., and Nourshargh, S. (2007). Getting to the site of
1395 inflammation: the leukocyte adhesion cascade updated. *Nat Rev Immunol* 7, 678–689.

1396 Lutz, R., and Bujard, H. (1997). Independent and Tight Regulation of Transcriptional Units in
1397 *Escherichia Coli* Via the LacR/O, the TetR/O and AraC/I1-I2 Regulatory Elements. *Nucleic*
1398 *Acids Res* 25, 1203–1210.

1399 Martinez, J.J., Mulvey, M.A., Schilling, J.D., Pinkner, J.S., and Hultgren, S.J. (2000). Type 1
1400 pilus-mediated bacterial invasion of bladder epithelial cells. *Embo J* 19, 2803–2812.

1401 Metzler, K.D., Fuchs, T.A., Nauseef, W.M., Reumaux, D., Roesler, J., Schulze, I., Wahn, V.,
1402 Papayannopoulos, V., and Zychlinsky, A. (2011). Myeloperoxidase is required for neutrophil
1403 extracellular trap formation: implications for innate immunity. *Blood* 117, 953–959.

1404 Mobley, H.L., Green, D.M., Trifillis, A.L., Johnson, D.E., Chippendale, G.R., Lockatell, C.V.,
1405 Jones, B.D., and Warren, J.W. (1990). Pyelonephritogenic *Escherichia coli* and killing of
1406 cultured human renal proximal tubular epithelial cells: role of hemolysin in some strains. *Infect*
1407 *Immun* 58, 1281–1289.

1408 Mulvey, M.A., Lopez-Boado, Y.S., Wilson, C.L., Roth, R., Parks, W.C., Heuser, J., and
 1409 Hultgren, S.J. (1998). Induction and Evasion of Host Defenses by Type 1-Piliated Uropathogenic
 1410 *Escherichia coli*. *Science* 282, 1494–1497.

1411 Mysorekar, I.U., and Hultgren, S.J. (2006). Mechanisms of uropathogenic *Escherichia coli*
 1412 persistence and eradication from the urinary tract. *Proc National Acad Sci* 103, 14170–14175.

1413 Nagamatsu, K., Hannan, T.J., Guest, R.L., Kostakioti, M., Hadjifrangiskou, M., Binkley, J.,
 1414 Dodson, K., Raivio, T.L., and Hultgren, S.J. (2015). Dysregulation of *Escherichia coli* α -
 1415 hemolysin expression alters the course of acute and persistent urinary tract infection. *Proc*
 1416 *National Acad Sci* 112, E871–E880.

1417 Nawroth, J.C., Lucchesi, C., Cheng, D., Shukla, A., Ngyuen, J., Shroff, T., Varone, A., Karalis,
 1418 K., Lee, H.-H., Alves, S., et al. (2020). A Microengineered Airway Lung Chip Models Key
 1419 Features of Viral-induced Exacerbation of Asthma. *Am J Resp Cell Mol* 63, 591–600.

1420 Nourshargh, S., Hordijk, P.L., and Sixt, M. (2010). Breaching multiple barriers: leukocyte
 1421 motility through venular walls and the interstitium. *Nat Rev Mol Cell Bio* 11, 366–378.

1422 Novak, R., Ingram, M., Marquez, S., Das, D., Delahanty, A., Herland, A., Maoz, B.M., Jeanty,
 1423 S.S.F., Somayaji, M.R., Burt, M., et al. (2020). Robotic fluidic coupling and interrogation of
 1424 multiple vascularized organ chips. *Nat Biomed Eng* 4, 407–420.

1425 Oliveira, S. de, Rosowski, E.E., and Huttenlocher, A. (2016). Neutrophil migration in infection
 1426 and wound repair: going forward in reverse. *Nat Rev Immunol* 16, 378–391.

1427 Papayannopoulos, V., Metzler, K.D., Hakkim, A., and Zychlinsky, A. (2010). Neutrophil
 1428 elastase and myeloperoxidase regulate the formation of neutrophil extracellular traps. *J Cell*
 1429 *Biology* 191, 677–691.

1430 Parekh, A., Cigan, A.D., Wognum, S., Heise, R.L., Chancellor, M.B., and Sacks, M.S. (2010).
 1431 Ex vivo deformations of the urinary bladder wall during whole bladder filling: Contributions of
 1432 extracellular matrix and smooth muscle. *J Biomech* 43, 1708–1716.

1433 Pascalis, R.D., Parnell, W.J., Abrahams, I.D., Shearer, T., Daly, D.M., and Grundy, D. (2018).
 1434 The inflation of viscoelastic balloons and hollow viscera. *Proc Royal Soc* 474, 20180102.

1435 Putrinš, M., Kogermann, K., Lukk, E., Lippus, M., Varik, V., and Tenson, T. (2015). Phenotypic
 1436 Heterogeneity Enables Uropathogenic *Escherichia coli* To Evade Killing by Antibiotics and
 1437 Serum Complement. *Infect Immun* 83, 1056–1067.

1438 Ronaldson-Bouchard, K., and Vunjak-Novakovic, G. (2018). Organs-on-a-Chip: A Fast Track
 1439 for Engineered Human Tissues in Drug Development. *Cell Stem Cell* 22, 310–324.

1440 Rossi, G., Manfrin, A., and Lutolf, M.P. (2018). Progress and potential in organoid research. *Nat*
 1441 *Rev Genet* 19, 671–687.

1442 Sato, T., Vries, R.G., Snippert, H.J., Wetering, M. van de, Barker, N., Stange, D.E., Es, J.H. van,
1443 Abo, A., Kujala, P., Peters, P.J., et al. (2009). Single Lgr5 stem cells build crypt-villus structures
1444 in vitro without a mesenchymal niche. *Nature* 459, 262–265.

1445 Schwartz, D.J., Chen, S.L., Hultgren, S.J., and Seed, P.C. (2011). Population Dynamics and
1446 Niche Distribution of Uropathogenic *Escherichia coli* during Acute and Chronic Urinary Tract
1447 Infection. *Infect Immun* 79, 4250–4259.

1448 Scott, V.C.S., Haake, D.A., Churchill, B.M., Justice, S.S., and Kim, J.-H. (2015). Intracellular
1449 Bacterial Communities: A Potential Etiology for Chronic Lower Urinary Tract Symptoms.
1450 *Urology* 86, 425–431.

1451 Shah, P., Fritz, J.V., Glaab, E., Desai, M.S., Greenhalgh, K., Frachet, A., Niegowska, M., Estes,
1452 M., Jäger, C., Seguin-Devaux, C., et al. (2016). A microfluidics-based in vitro model of the
1453 gastrointestinal human–microbe interface. *Nat Commun* 7, 11535.

1454 Si, L., Bai, H., Rodas, M., Cao, W., Oh, C.Y., Jiang, A., Moller, R., Hoagland, D., Oishi, K.,
1455 Horiuchi, S., et al. (2021). A human-airway-on-a-chip for the rapid identification of candidate
1456 antiviral therapeutics and prophylactics. *Nat Biomed Eng* 1–15.

1457 Smith, Y.C., Grande, K.K., Rasmussen, S.B., and O'Brien, A.D. (2006). Novel Three-
1458 Dimensional Organoid Model for Evaluation of the Interaction of Uropathogenic *Escherichia*
1459 *coli* with Terminally Differentiated Human Urothelial Cells. *Infect Immun* 74, 750–757.

1460 Sokurenko, E.V., Vogel, V., and Thomas, W.E. (2008). Catch-Bond Mechanism of Force-
1461 Enhanced Adhesion: Counterintuitive, Elusive, but ... Widespread? *Cell Host Microbe* 4, 314–
1462 323.

1463 Solis, A.G., Bielecki, P., Steach, H.R., Sharma, L., Harman, C.C.D., Yun, S., Zoete, M.R. de,
1464 Warnock, J.N., To, S.D.F., York, A.G., et al. (2019). Mechanosensation of cyclical force by
1465 PIEZO1 is essential for innate immunity. *Nature* 573, 69–74.

1466 Song, J., Duncan, M.J., Li, G., Chan, C., Grady, R., Stapleton, A., and Abraham, S.N. (2007). A
1467 Novel TLR4-Mediated Signaling Pathway Leading to IL-6 Responses in Human Bladder
1468 Epithelial Cells. *Plos Pathog* 3, e60.

1469 Spaulding, C.N., Klein, R.D., Ruer, S., Kau, A.L., Schreiber, H.L., Cusumano, Z.T., Dodson,
1470 K.W., Pinkner, J.S., Fremont, D.H., Janetka, J.W., et al. (2017). Selective depletion of
1471 uropathogenic *E. coli* from the gut by a FimH antagonist. *Nature* 546, 528–532.

1472 Suzuki, K., Koyanagi-Aoi, M., Uehara, K., Hinata, N., Fujisawa, M., and Aoi, T. (2019).
1473 Directed differentiation of human induced pluripotent stem cells into mature stratified bladder
1474 urothelium. *Sci Rep-Uk* 9, 10506.

1475 Thacker, V.V., Dhar, N., Sharma, K., Barrile, R., Karalis, K., and McKinney, J.D. (2020). A
1476 lung-on-chip model of early *M. tuberculosis* infection reveals an essential role for alveolar
1477 epithelial cells in controlling bacterial growth. *Elife* 9, e59961.

1478 Thacker, V.V., Sharma, K., Dhar, N., Mancini, G., Sordet-Dessimoz, J., and McKinney, J.D.
1479 (2021). Rapid endotheliitis and vascular damage characterize SARS-CoV-2 infection in a human
1480 lung-on-chip model. *Embo Rep* 22, e52744.

1481 Tovaglieri, A., Sontheimer-Phelps, A., Geirnaert, A., Prantil-Baun, R., Camacho, D.M., Chou,
1482 D.B., Jalili-Firoozinezhad, S., Wouters, T. de, Kasendra, M., Super, M., et al. (2019). Species-
1483 specific enhancement of enterohemorrhagic *E. coli* pathogenesis mediated by microbiome
1484 metabolites. *Microbiome* 7, 43.

1485 Truschel, S.T., Wang, E., Ruiz, W.G., Leung, S.-M., Rojas, R., Lavelle, J., Zeidel, M., Stoffer,
1486 D., and Apodaca, G. (2002). Stretch-regulated Exocytosis/Endocytosis in Bladder Umbrella
1487 Cells. *Mol Biol Cell* 13, 830–846.

1488 Wang, E.C.Y., Lee, J.-M., Ruiz, W.G., Balestreire, E.M., Bodungen, M. von, Barrick, S.,
1489 Cockayne, D.A., Birder, L.A., and Apodaca, G. (2005). ATP and purinergic receptor–dependent
1490 membrane traffic in bladder umbrella cells. *J Clin Invest* 115, 2412–2422.

1491 Wang, J., Wang, C., Xu, N., Liu, Z.-F., Pang, D.-W., and Zhang, Z.-L. (2019). A virus-induced
1492 kidney disease model based on organ-on-a-chip: Pathogenesis exploration of virus-related renal
1493 dysfunctions. *Biomaterials* 219, 119367.

1494 Yang, E., Chee, J.L.Y., Duraiswamy, S., Chen, S., Lees, K., and Chen, S.L. (2019). Isolation of
1495 Single Intracellular Bacterial Communities Generated from a Murine Model of Urinary Tract
1496 Infection for Downstream Single-cell Analysis. *J Vis Exp Jove*.

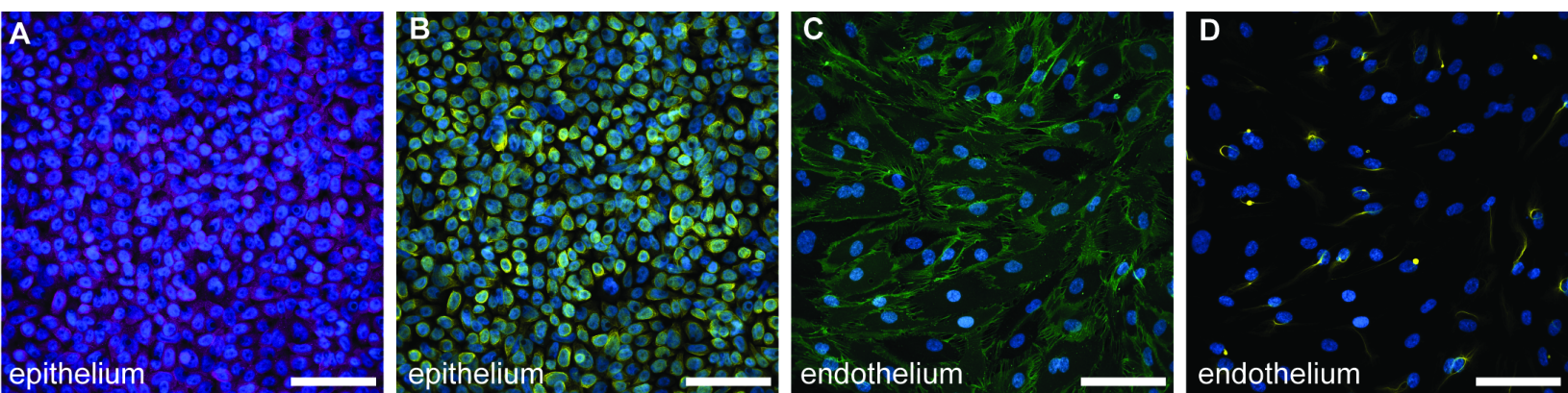
1497 Yu, Y., Kwon, K., Tsitrin, T., Bekele, S., Sikorski, P., Nelson, K.E., and Pieper, R. (2017).
1498 Characterization of Early-Phase Neutrophil Extracellular Traps in Urinary Tract Infections. *Plos*
1499 *Pathog* 13, e1006151.

1500 Zahler, S., Kowalski, C., Brosig, A., Kupatt, C., Becker, B.F., and Gerlach, E. (1997). The
1501 function of neutrophils isolated by a magnetic antibody cell separation technique is not altered in
1502 comparison to a density gradient centrifugation method. *J Immunol Methods* 200, 173–179.

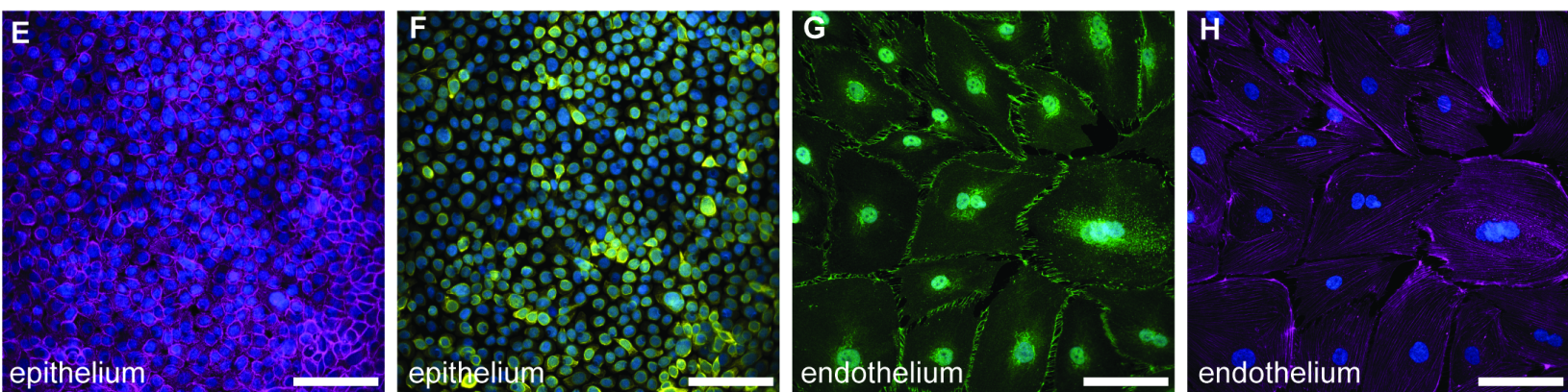
1503 Zalewska-Piątek, B., Olszewski, M., Lipniacki, T., Błoński, S., Wieczór, M., Bruździak, P.,
1504 Skwarska, A., Nowicki, B., Nowicki, S., and Piątek, R. (2020). A shear stress micromodel of
1505 urinary tract infection by the *Escherichia coli* producing Dr adhesin. *Plos Pathog* 16, e1008247.

1506 Zhou, M., Zhang, X., Wen, X., Wu, T., Wang, W., Yang, M., Wang, J., Fang, M., Lin, B., and
1507 Lin, H. (2016). Development of a Functional Glomerulus at the Organ Level on a Chip to Mimic
1508 Hypertensive Nephropathy. *Sci Rep-Uk* 6, 31771.

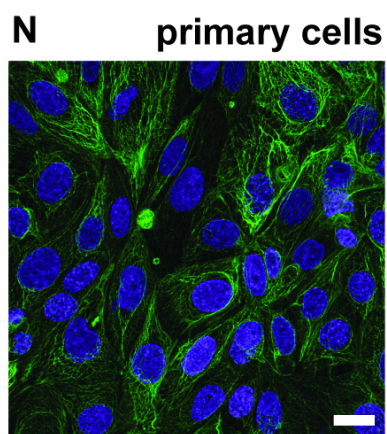
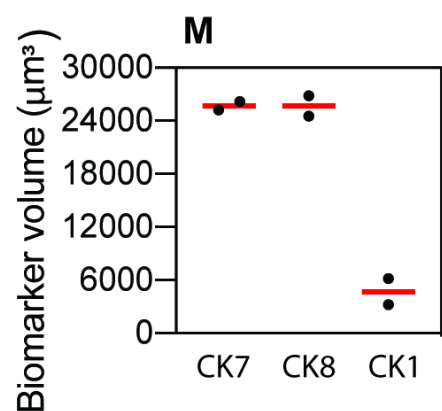
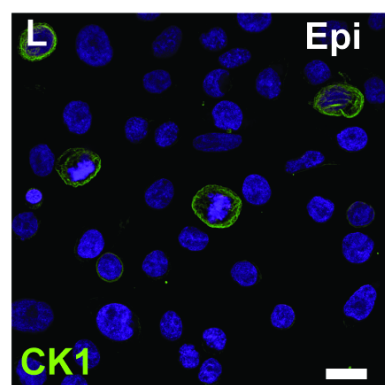
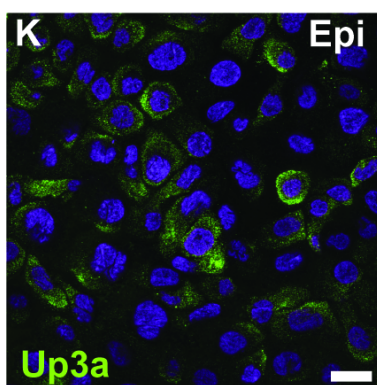
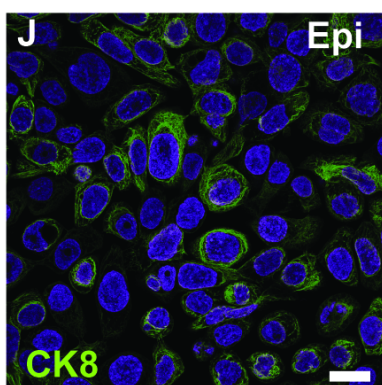
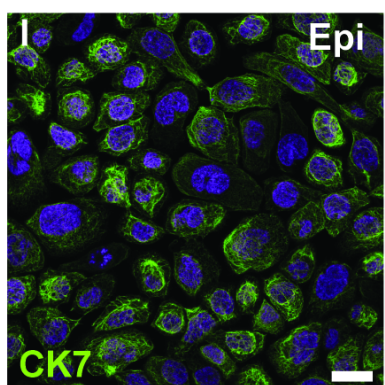
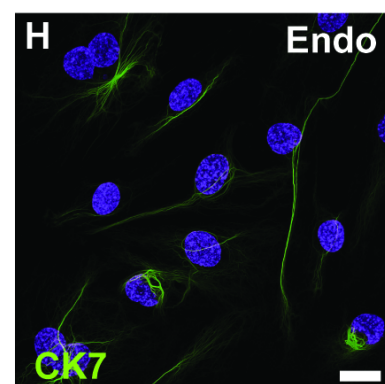
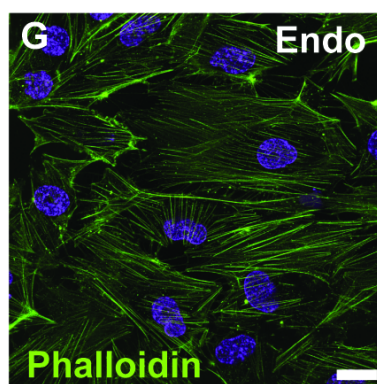
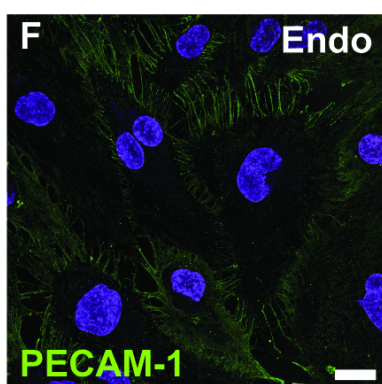
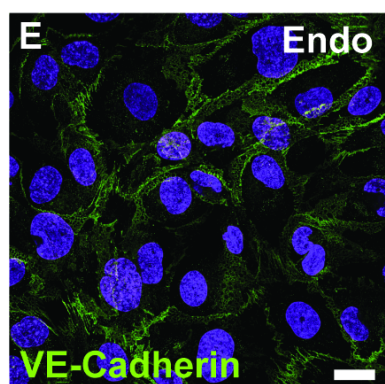
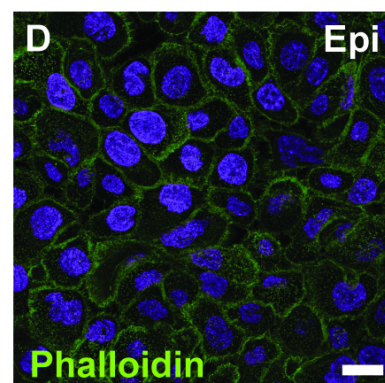
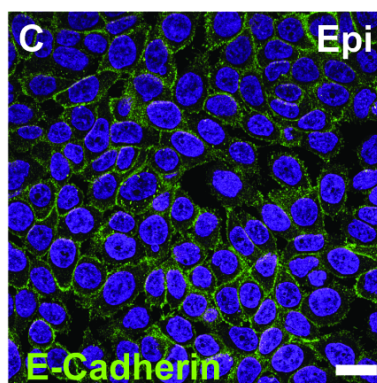
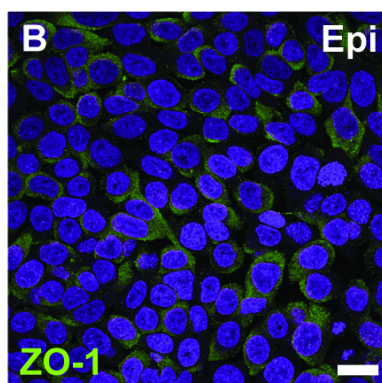
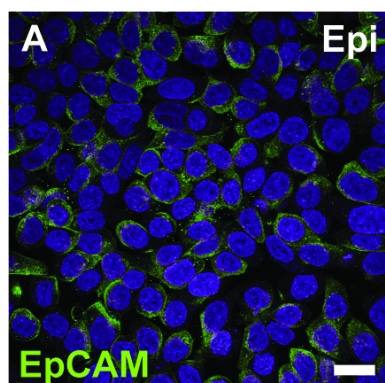
1509

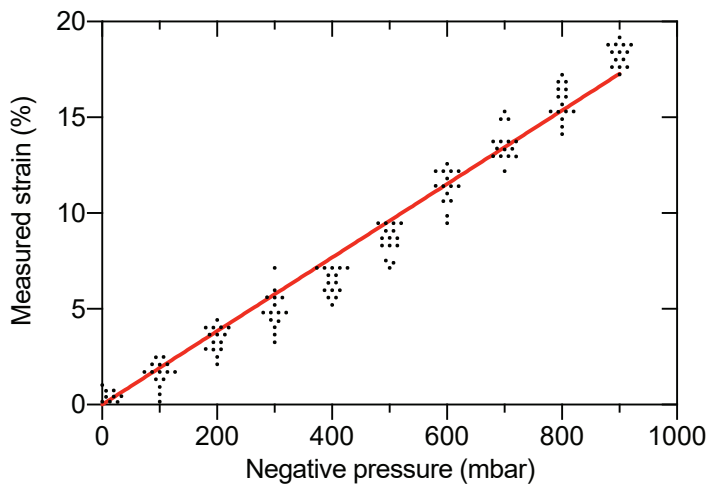


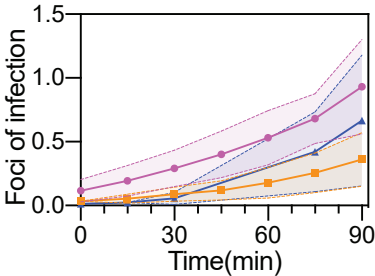
A-D: ■ EpCAM ■ CK7 ■ PECAM1 ■ DAPI

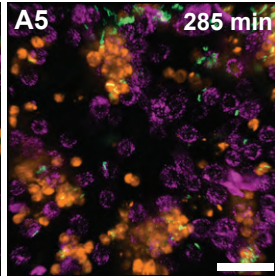
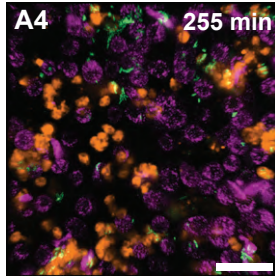
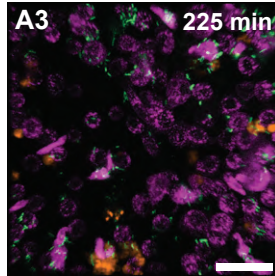
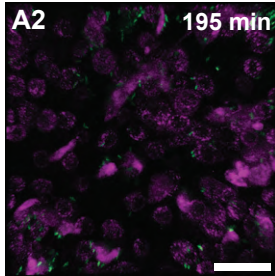
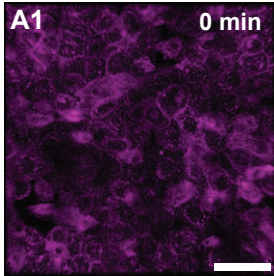


E-H: ■ Actin ■ CK8 ■ VE-Cadherin ■ DAPI

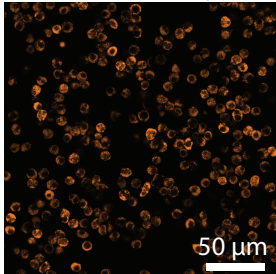




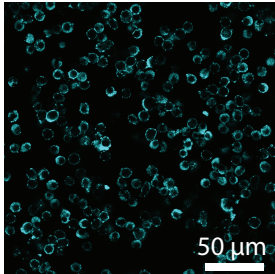




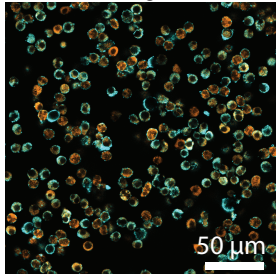
A Cell Tracker Deep Red



B CD 15



C merged



A. uninfected control + neutrophils



100 μ m

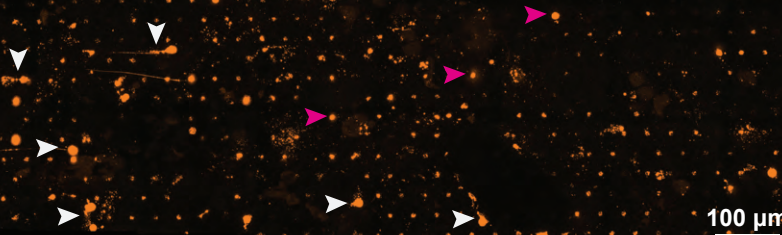


B. uninfected control (brightfield)

100 μ m



C. UPEC infection + neutrophils



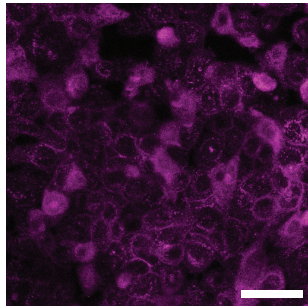
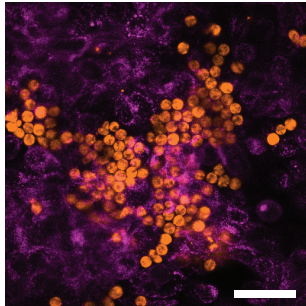
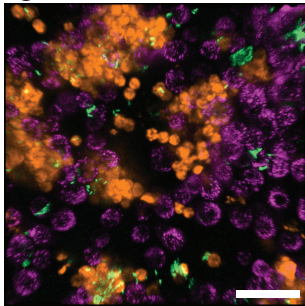
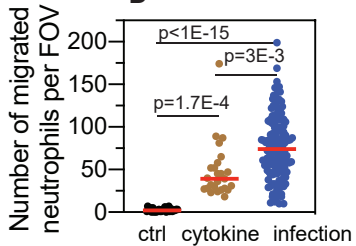
100 μ m

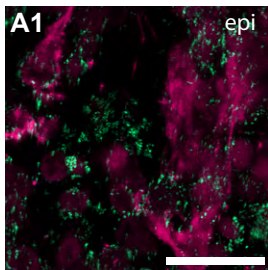


D. UPEC infection (brightfield)

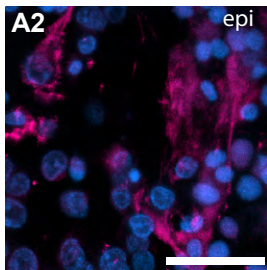
100 μ m



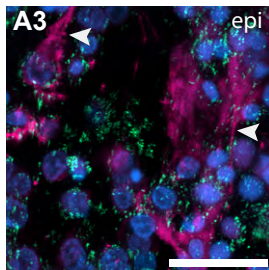
A**uninfected control****B****cytokine****C****UPEC infection****D**



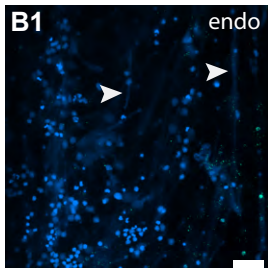
UPEC Anti-Myeloperoxidase



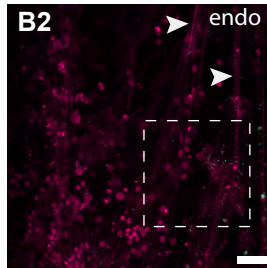
DAPI



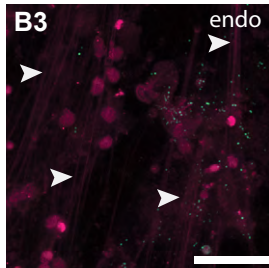
Merged

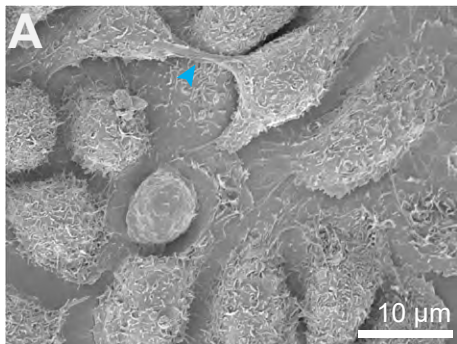


UPEC DAPI

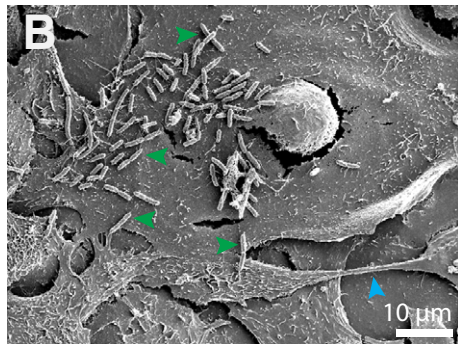


Anti-Neutrophil Elastase

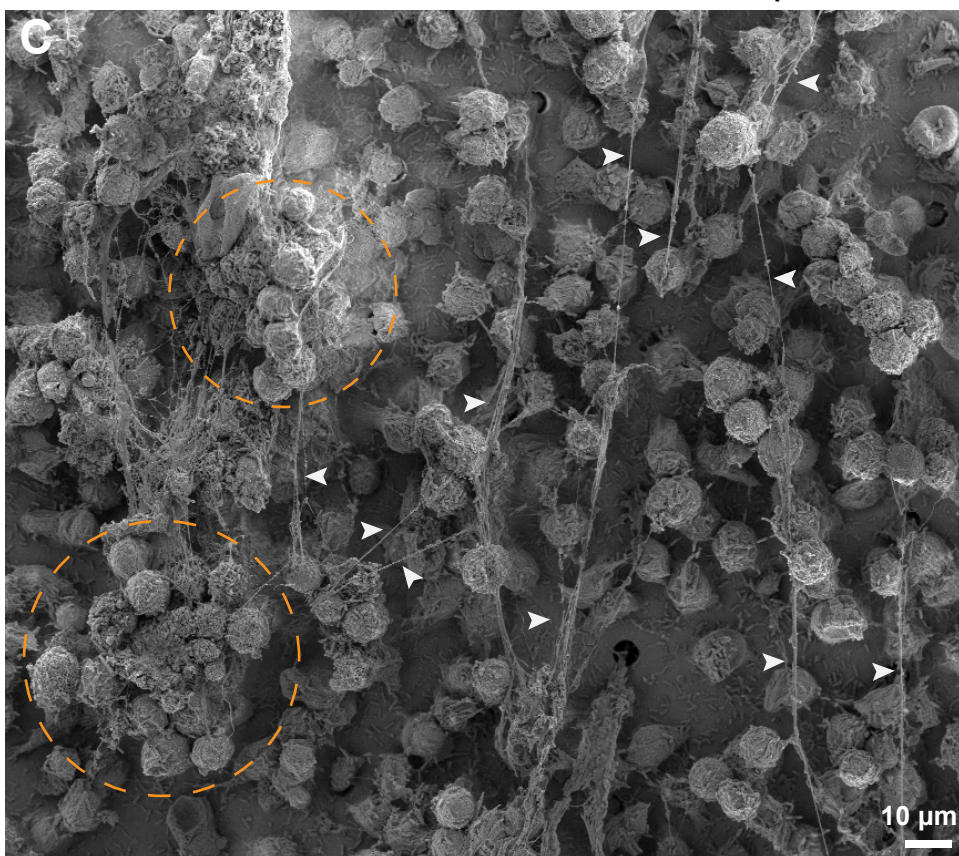




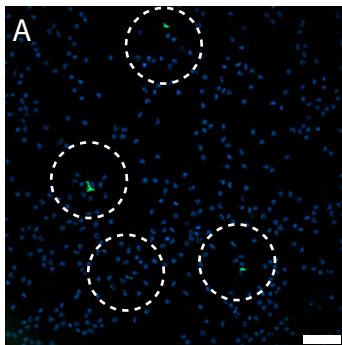
uninfected bladder-chip



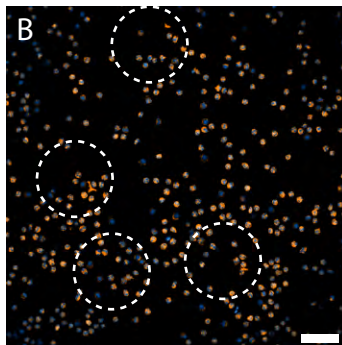
**infected bladder-chip
without neutrophils**



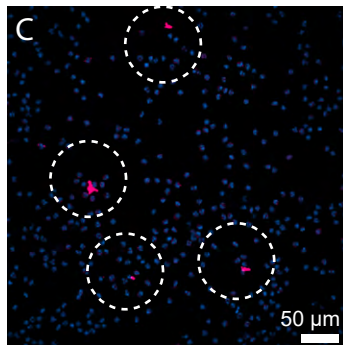
NETs in infected bladder-chip



DAPI + UPEC

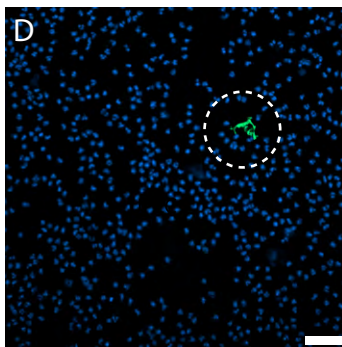


CellTracker

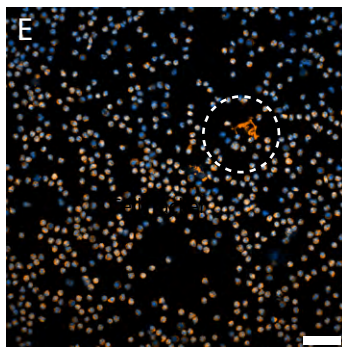


Anti-Myeloperoxidase

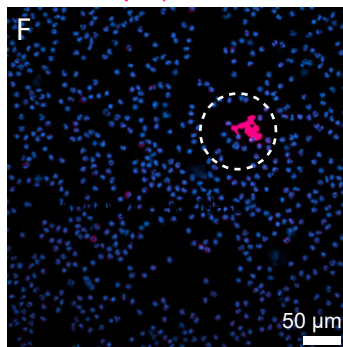
50 μ m



DAPI + UPEC

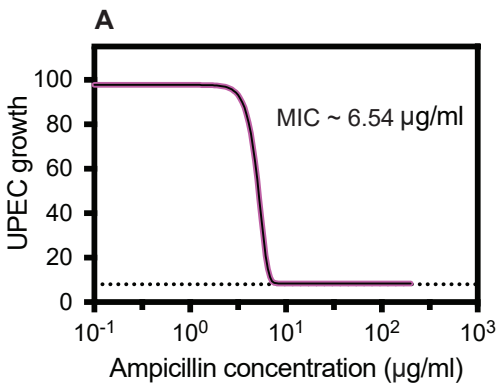


CellTracker

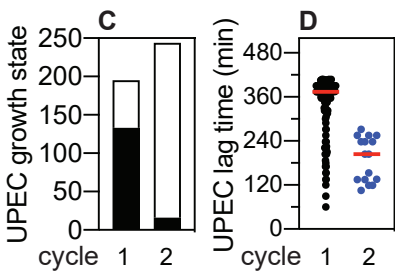
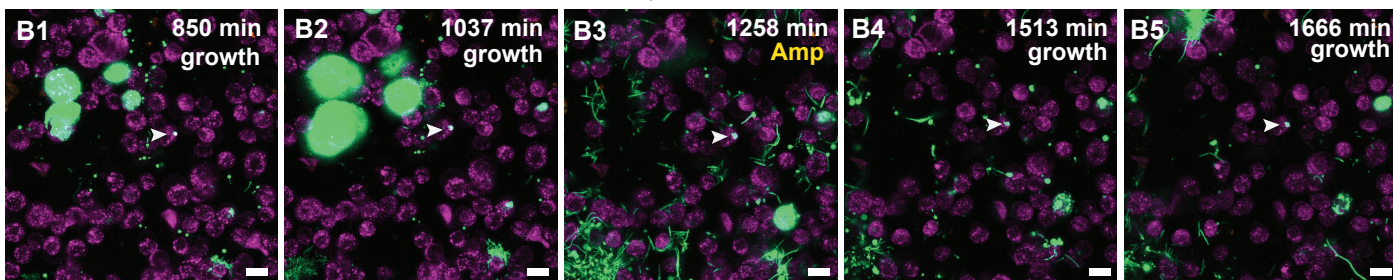


Anti-Neutrophil Elastase

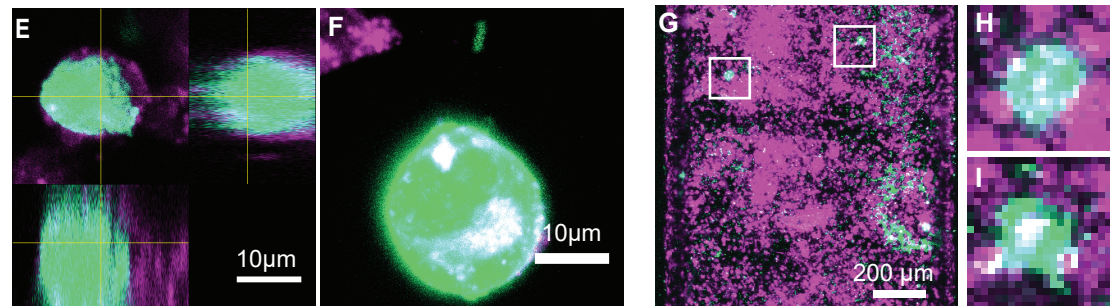
50 μ m

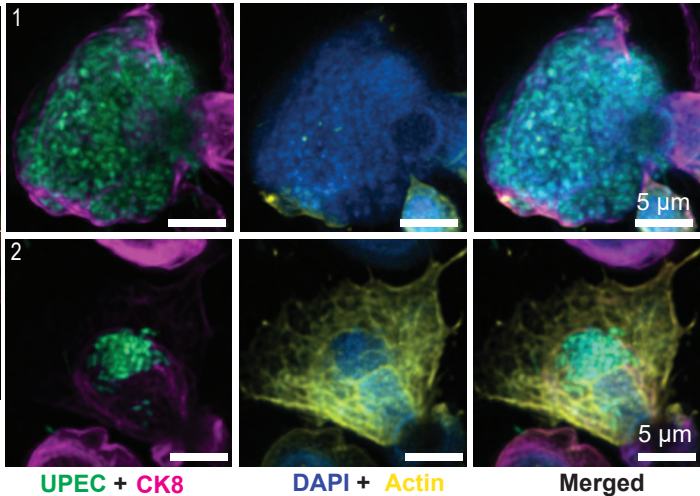
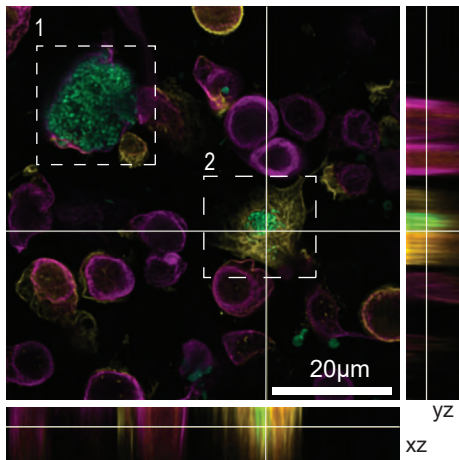


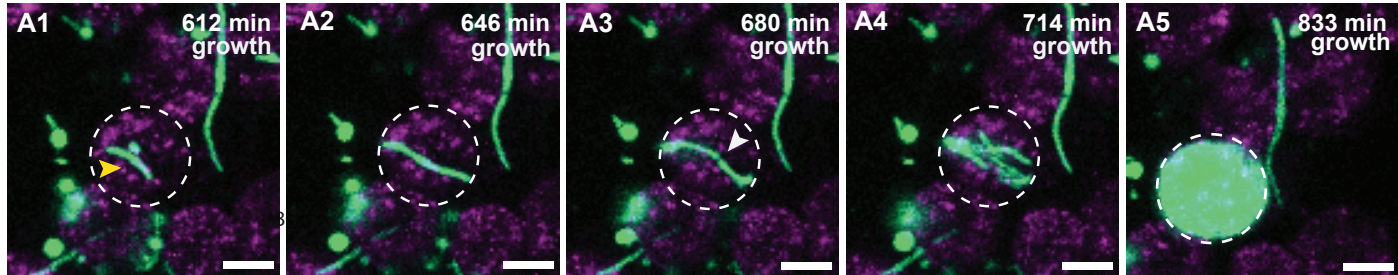
Ampicillin treatment

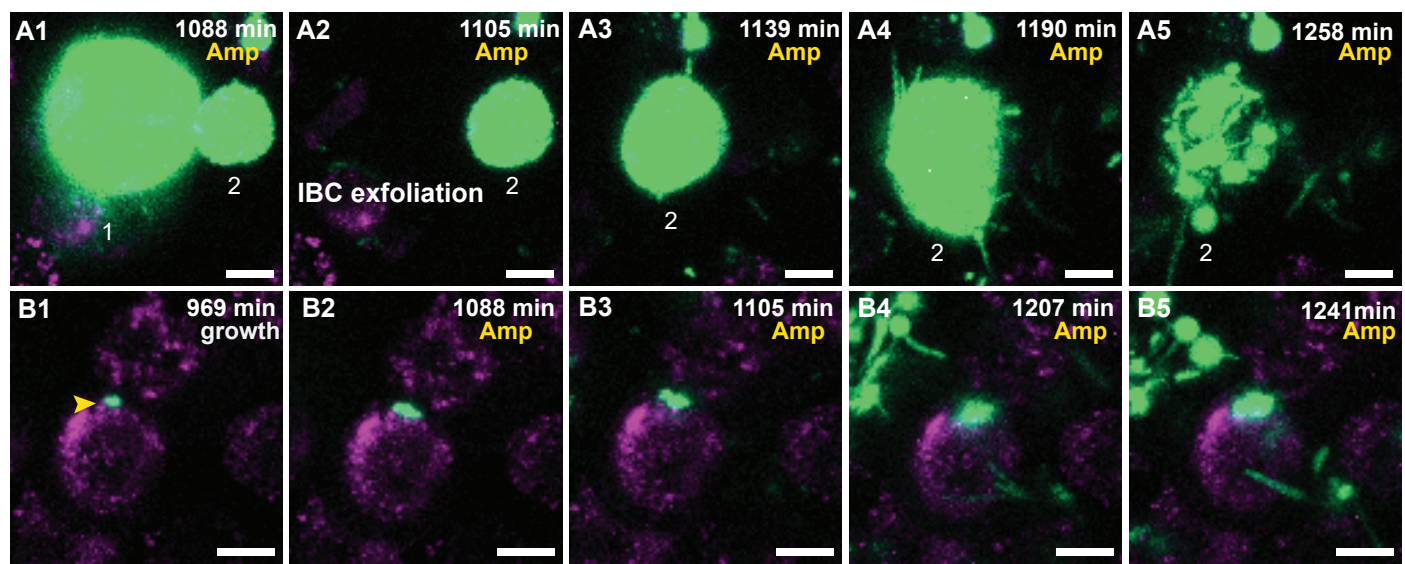


Fosfomycin treatment - primary epithelial cells



A





Primary bladder epithelial cells

UPEC infection
(2 hours)

Fosfomycin
(3 hours)

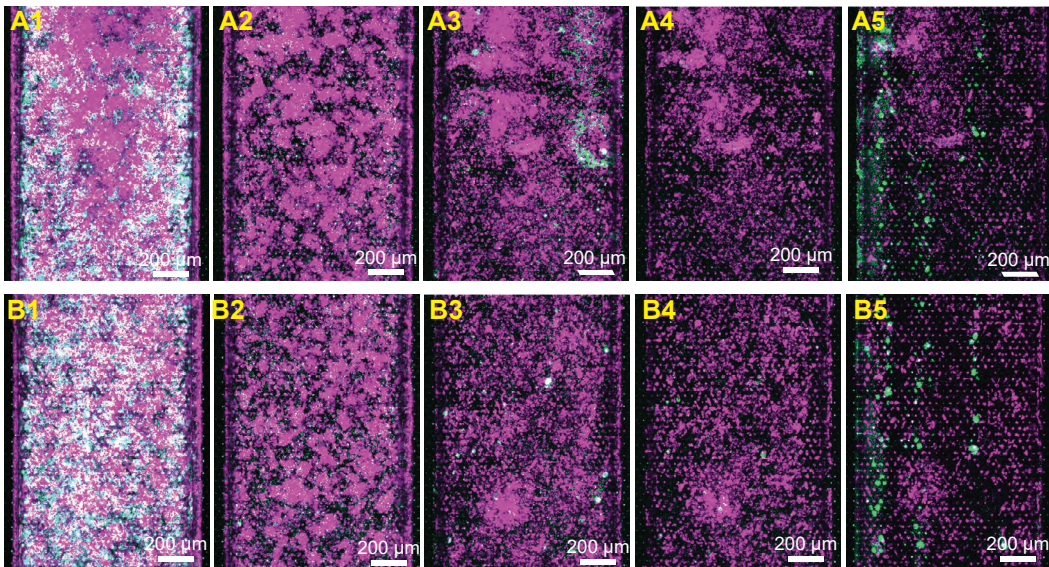
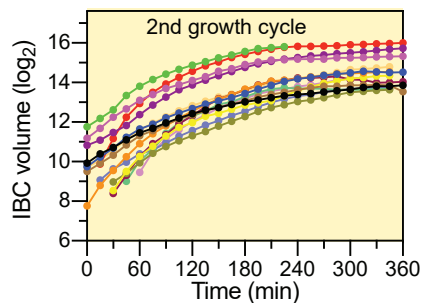
Growth cycle 1
(6 hours)

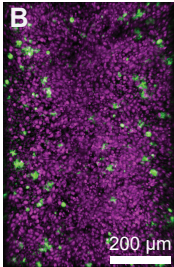
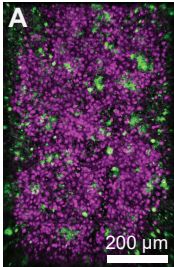
Fosfomycin
(3 hours)

Growth cycle 2
(6 hours)

5637 epithelial cells

C





Duty cycle (+)

Duty cycle(-)